

WRISTP²: A Wrist-Worn System for Hand Pose and Pressure Estimation

Ziheng Xi*

Department of Automation, BNRIST,
Tsinghua University
Beijing, China
xizh21@mails.tsinghua.edu.cn

Zihang Ao*

Department of Automation, Tsinghua
University
Beijing, China
azh24@mails.tsinghua.edu.cn

Yitao Wang

Department of Automation, Tsinghua
University
Beijing, China
wangyita23@mails.tsinghua.edu.cn

Mingze Gao

Tsinghua University
Beijing, China
gaomingze2022@gmail.com

Wanmei Zhang

Tsinghua University
Beijing, China
zwm23@mails.tsinghua.edu.cn

Jianjiang Feng

Department of Automation, Tsinghua
University
Beijing, China
jfeng@tsinghua.edu.cn

Jie Zhou

Department of Automation, BNRIST,
Tsinghua University
Beijing, China
jzhou@tsinghua.edu.cn

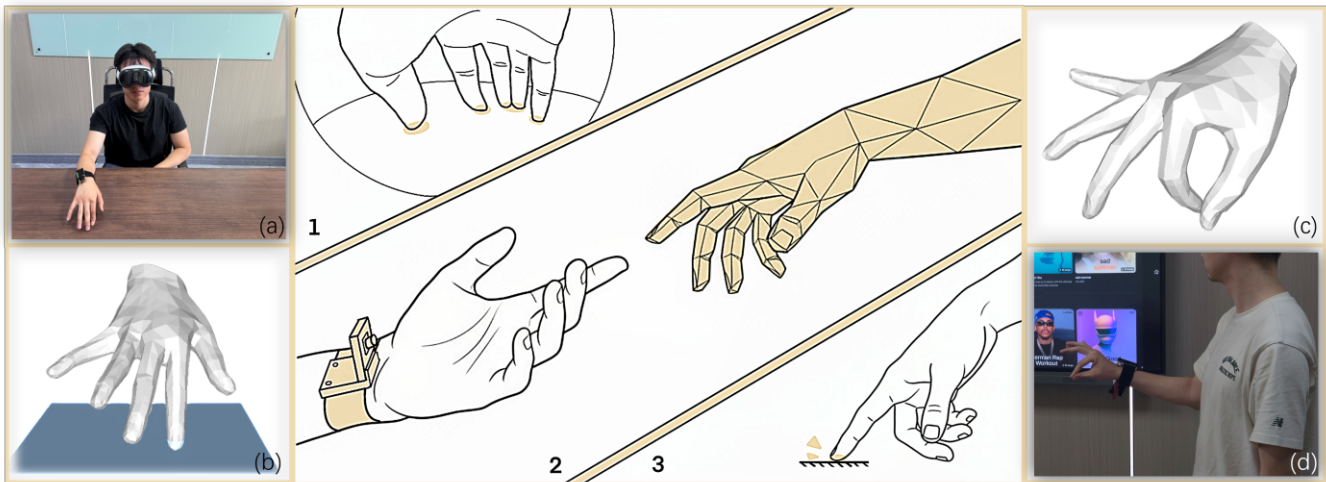


Figure 1: WRISTP² is a wrist-worn system with a wide-FOV fisheye camera that reconstructs 3D hand pose and per-vertex pressure in real time. Illustrated scenarios: (a) planar input on a virtual surface in XR; (b) reconstructed hand and planar contact corresponding to (a); (c) reconstructed hand corresponding to (d); (d) controlling slide presentations in a mobile scenario.

Abstract

Accurate 3D hand pose and pressure sensing is essential for immersive human-computer interaction, yet simultaneously achieving both in mobile scenarios remains a significant challenge. We present

*These authors contributed equally to this work.



This work is licensed under a Creative Commons Attribution 4.0 International License.
CHI '26, Barcelona, Spain

© 2026 Copyright held by the owner/author(s).
ACM ISBN 979-8-4007-2278-3/2026/04
<https://doi.org/10.1145/3772318.3790626>

WRISTP², a camera-based wrist-worn system that estimates 3D hand pose and per-vertex pressure from a single wide-FOV RGB frame in real time. A ViT (Vision Transformer) backbone with joint-aligned tokens predicts Hand-VQ-VAE codebook indices for mesh recovery, while an extrinsics-conditioned branch jointly estimates per-vertex pressure. On a self-collected dataset of 133,000 frames (20 subjects; 48 on-plane and 28 mid-air gestures), WRISTP² attains MPJPE (Mean Per-Joint Position Error) of 2.9 mm, Contact IoU of 0.712, Vol. IoU of 0.618, and foreground pressure MAE of 10.4 g. Across three user studies, WRISTP² delivers touchpad-level efficiency in mid-air pointing and robust multi-finger pressure control on an uninstrumented

desktop. In a real-world large-display Whac-A-Mole task, WRISTP² also enables higher success ratio and lower arm fatigue than head-mounted camera-based baselines. These results position WRISTP² as an effective, mobile solution for versatile pose- and pressure-based interaction. Website: <https://zhenqis123.github.io/WristPP/>

CCS Concepts

• **Human-centered computing** → **Human computer interaction (HCI)**; • **Computing methodologies** → *Computer vision*; • **Hardware** → Wearable and mobile devices; • **Applied computing** → Multimedia systems.

Keywords

Hand Pose Estimation, Pressure Estimation, Human-Computer Interaction, Wearable Devices, Interactive Systems

ACM Reference Format:

Ziheng Xi, Zihang Ao, Yitao Wang, Mingze Gao, Wanmei Zhang, Jianjiang Feng, and Jie Zhou. 2026. WRISTP²: A Wrist-Worn System for Hand Pose and Pressure Estimation. In *Proceedings of the 2026 CHI Conference on Human Factors in Computing Systems (CHI '26), April 13–17, 2026, Barcelona, Spain*. ACM, New York, NY, USA, 30 pages. <https://doi.org/10.1145/3772318.3790626>

1 Introduction

Accurate perception of hand pose and applied pressure is crucial for immersive, natural, and efficient interaction, especially in egocentric settings [45, 80, 107]. In extended reality (XR), pose alone is often insufficient: touch contact and pressure provide additional control bandwidth and feedback [7]. For example, when writing or drawing on a virtual canvas, variation in finger pressure and contact area can modulate stroke thickness [21]. In virtual piano playing, different finger pressures and poses can produce various sound effects such as soft, loud, vibrato, and staccato notes [31]. Many laptops already feature pressure-sensitive touchpads that respond to different force levels with haptic feedback, underscoring the practical value of pressure-aware interaction.

At the same time, building a system that senses both rich 3D hand pose and fine-grained pressure in everyday settings remains challenging. Key difficulties include: (i) the large number of hand joints and the resulting articulatory complexity; (ii) out-of-view (OOV) and occlusion events during natural interaction; and (iii) the acquisition of high-resolution contact and pressure data that generalizes beyond instrumented surfaces.

Environment-mounted systems—such as depth cameras [65, 68], multi-camera arrays [42, 67, 102], and optical motion capture (MoCap) systems [4, 54]—provide high-accuracy pose, but typically focus on geometry alone and require fixed workspaces, careful calibration, and non-trivial deployment cost and space. Glove-based wearables equipped with flexible sensors [11, 70] can directly measure pose and pressure, yet often reduce comfort, interfere with tactile perception, and restrict finger motion. Lightweight on-body solutions based on inertial measurement units (IMUs) [83, 89, 92], electromyography (EMG) [37, 39, 82], and acoustic sensing [49, 90] bring sensing closer to the hand, but are often limited to recognizing predefined gesture sets without continuous 3D articulation [44, 49, 82, 92], or cannot estimate pressure [30].

Head-mounted displays (HMDs) provide egocentric visual access to the hands and underpin commercial hand tracking [10, 50]. However, hands generally need to operate within the headset's tracking volume to remain reliably trackable, which can be challenging near the edges of the field of view and during prolonged mid-air pointing [91, 107]. From the HMD perspective, it is also difficult to distinguish whether the hand is hovering just above a surface or in actual contact [64]. In addition, HMDs tend to have higher cost and power consumption, which can limit everyday adoption.

Recent prototypes and products based on wrist-mounted cameras [5, 27, 33, 51, 103, 109] suggest an alternative: wrist-anchored, eyes-free sensing that moves with the user. But these devices provide only limited hand pose estimation and, to our knowledge, do not estimate hand pressure. Achieving high-precision 3D pose and pressure estimation with a portable, low-cost device, especially under complex finger motions in mobile scenarios, remains an open challenge.

We present WRISTP², a wrist-mounted system that reconstructs hand pose and per-vertex contact and pressure in real time from a single wide-FOV (Field-Of-View) fisheye RGB frame. The system employs a deep neural network to recover an accurate 3D hand mesh and surface-pressure distribution, enabling precise, multidimensional input. With these outputs, WRISTP² turns rigid planar or quasi-planar surfaces into touchpad-like, pressure-sensitive input areas and also supports fine-grained mid-air gestures, broadening the space of mobile and XR interaction.

We designed 48 plane-based and 28 mid-air gestures, and collected a dataset of 133,000 frames from 20 participants. The data collection system consists of an infrared FZMotion Motion Capture System, a Kinect camera, and a Sensel Morph [86] pressure-sensitive pad, enabling the acquisition of sub-millimeter marker positions and pressure maps. High-fidelity 3D hand meshes and per-vertex pressure annotations were then obtained through a multi-objective optimization process. Building on this dataset, we propose a novel framework that tokenizes the ground-truth 3D hand mesh into a discrete latent space with Hand-VQ-VAE, then leverages a ViT (Vision Transformer) [106] based neural network to predict the corresponding token indices in the codebook to get hand mesh prediction. In parallel, the per-vertex surface pressure distribution is inferred through a cross-attention mechanism. The results show that the mean per-joint position error (MPJPE) was 2.9 mm, the mean joint angle error (MJAE) was 3.2°, the intersection over union (IoU) for pressure was 71.2%, the volume intersection over union (Vol.IoU) for surface pressure was 61.8%, the mean absolute error (MAE) on single vertex with positive value was 10.4 g. To assess the practical applicability of WRISTP² for human-computer interaction (HCI), we conducted three user studies spanning both planar and mid-air interaction. Across the three studies, WRISTP² delivered input efficiency comparable to standard input devices and robust performance on demanding tasks requiring fine-grained pressure and displacement control. In an additional application study, we compared WRISTP² with head-mounted camera-based input methods in a real-world large-screen interaction task; participants using WRISTP² completed the task more effectively and reported lower arm fatigue. In user-experience questionnaires, participants

also highlighted the naturalness and accuracy of interaction with WRISTP².

In summary, our main contributions include:

- We introduce WRISTP², an eyes-free, low-cost, wide-FOV wrist-worn device that enables high-precision hand pose and pressure estimation.
- We collect a large-scale dataset of wrist-mounted fisheye images with aligned hand meshes and surface pressure, and design an extrinsics-aware Hand-VQ-VAE based architecture for joint pose and pressure prediction.
- We extensively evaluate WRISTP² through offline experiments and four studies. WRISTP² achieves low-millimeter pose and high pressure accuracy, and delivers touchpad-level pointing efficiency and robust multi-finger pressure control (Studies 1–3), and, in a large-display Whac-A-Mole task (Study 4), yields higher task success and lower arm fatigue than head-mounted baselines.

2 Related Work

Accurate hand pose and pressure estimation underpins immersive human-computer interaction. Beyond algorithmic design, a system’s capability is strongly influenced by its sensing placement, which determines (i) what cues are observable, (ii) whether hands remain continuously trackable through natural postures, and (iii) how ergonomic and deployable the interaction is. We therefore organize related work by placement—environment-mounted, head-mounted (egocentric), and wrist-proximal—and, within each, discuss pose and pressure jointly as two facets of hand understanding. Representative methods and performance appear in Table 1.

2.1 Environment-Mounted Sensing

Environment-mounted systems observe from fixed external viewpoints or instrument the world itself. For pose, classical geometric pipelines combine calibrated multi-view/depth/IR with triangulation, kinematic fitting, and optimization [54, 71, 95, 96, 111], which enabled high-accuracy capture and the creation of canonical benchmarks—NYU [99], ICVL [97], STB [55], BigHand2.2M [114], etc [18, 67, 122]. Learning-based third-person vision then regresses joints and meshes directly from RGB or depth using heatmaps [19, 66], volumetric encoding [121], occlusion-aware modeling for hand-object interaction [8, 9], and end-to-end MANO-based reconstruction with CNNs and transformers [1, 46, 69, 73, 75, 76]. For pressure, two strategies dominate: (a) instrumented surfaces such as force/pressure mats [41, 98, 104], fingertip sensors [2, 77], or tactile-sensing gloves [94] directly measure pressure distributions but alter surfaces or require worn hardware; (b) external visual inference, where pressure is estimated from color changes [6, 57, 58], soft-tissue deformation [32], and cast shadows [28, 29]. Other approaches infer force through object-motion cues during grasping [15, 52, 74]. Dataset-driven methods further pair RGB with high-resolution pressure maps from Sensel Morph [86] to learn appearance-to-pressure mappings [21, 22].

However, these systems inherently confine interaction to instrumented workspaces. The reliance on fixed camera frustums and complex calibration creates a high deployment burden and severely restricts mobility. Furthermore, external viewpoints are

susceptible to frequent occlusions and out-of-view motions, which break both pose tracking and visual pressure inference pipelines. Finally, methods that infer force via object motion are fundamentally inapplicable to interactions with static surfaces (e.g., tables, walls). Collectively, these constraints render environment-mounted sensing unsuitable for ubiquitous, everyday scenarios.

2.2 Head-Mounted Sensing

Head-mounted cameras co-locate sensing with head, yielding long-horizon hand visibility and stable reference frames in mixed reality; this configuration underpins commercial hand tracking (e.g., Meta Quest) [61] and research systems that unify multi-view egocentric imagery with end-to-end 3D hand reconstruction [24].

Beyond pose, egocentric viewpoints expose contact appearance on visible skin, enabling pressure inference from purely visual cues. In particular, estimating fingertip pressure from local tissue deformation and shading demonstrates appearance-to-pressure mappings in the wild [64], while jointly estimating hand mesh and pressure shows bidirectional benefits between geometry and contact intensity [117].

Recent work broadens egocentric pressure and touch beyond fingertips to broader contact regions and tasks. Real-time index-to-palm touch with single head-mounted RGB illustrates monocular pressure-sensitive interaction on the palm [25]; uncertainty-aware egocentric pipelines support rapid touch and text input in MR by explicitly modeling confidence [93]; egocentric sequences enable thumb-tip force estimation during everyday manipulation [36]; and hand-bound pads demonstrate pressure-like input using hand-tracking signals alone, without instrumented surfaces [13].

While egocentric cameras offer rich cues of hands, they inherently restrict observability to the HMD’s limited FOV. This creates a usability dilemma: ensuring reliable tracking requires users to maintain hands within the specific volume, forcing elevated postures that induce "gorilla-arm" fatigue [12, 26, 35]. Conversely, resting hands naturally outside this frustum causes immediate out-of-view (OOV) failures, breaking both pose and pressure estimation [20, 78, 91]. Consequently, interaction is fundamentally bound by the user’s head orientation.

Commercial HMDs partly mitigate these constraints by deploying multiple sensors to enlarge the tracking volume. However, even distinct multi-camera setups struggle to observe hands in natural resting positions (e.g., alongside the body) due to torso occlusion. This limitation is exacerbated by the parallel trend toward lightweight, glasses-style devices [62, 63, 79], where strict hardware budgets often restrict sensing to a single, narrow-FOV camera. In both regimes, hands frequently exit the visible frustum; specifically addressing this "hands-down" blind spot is critical for ubiquitous interaction.

2.3 Wrist-Proximal Sensing

Wrist-Proximal On-body sensing moves perception with the user, improving continuity through natural postures and reducing reliance on external infrastructure. Non-optical wearables (EMG [39, 82, 87], acoustics [34, 49, 113], capacitive [101], IR laser/tomography [43, 59], electrical impedance [115, 116], IMU [88]) bring sensors near the hand. These modalities offer promising continuous tracking

Table 1: Hand pose and pressure estimation techniques that have been proposed or hold potential applications in HCI, as well as the performance metrics achieved on their own datasets. Here, “○” indicates that the technique supports partial hand mesh estimation for pose or pressure, limited to keypoints, wrist points, individual fingers, or other localized hand positions. “_” signifies that the corresponding metric is not reported in the paper, or the technique required to achieve this metric is not implemented in the paper.

Category	Study	Year	Sensor	Eyes-free	Hand Pose Estimation	Contact Detection	Hand Pressure Estimation	Pose MPJPE(mm) _↓	Pose MJAE(°) _↓	Contact Accuracy(%) _↑	Pressure MAE(kPa/%g) _↓
Head-worn	EgoTouch [64]	2024	HMD	×	×	✓	○	–	–	95.6	5.6-16.4%
	PressureVision++ [21]	2024	HMD	×	×	✓	✓	–	–	89.3	44 kPa
	EgoPressure [117]	2024	HMD	×	✓	✓	✓	5.68	–	92	71 kPa
Arm-worn	PiMForce [87]	2024	EMG+RGB camera	×	×	×	○	–	–	–	6.98-10.1%
	EITPose [47]	2024	EIT sensor	✓	✓	×	×	11.06-18.91	–	–	–
Hand-worn	VibeMesh [56]	2024	microphone+ speaker+RGB-D camera	×	✓	✓	×	–	–	–	–
	Ring-a-Pose [113]	2024	microphone + speaker	✓	○	×	×	10.30-14.10	–	–	–
Wrist-worn	Digits [43]	2012	IR camera	✓	○	×	×	–	5.34-7.51	–	–
	WristCam [5]	2019	RGB camera	✓	○	×	×	–	–	–	–
	FingerTrak [27]	2020	IR camera	✓	✓	×	×	12.6	6.46	–	–
	Back-Hand-Pose [109]	2020	IR camera	✓	○	×	×	–	8.81-9.77	–	–
	RotoWrist [81]	2021	IR light modules	✓	○	×	×	–	5.9-7.8	–	–
	emg2pose [82]	2024	EMG	✓	✓	×	×	15.8-27.2	12.2-15.8	–	–
	EchoWrist [49]	2024	microphone + speaker	✓	○	×	×	4.81	3.79	–	–
	FineType [51]	2025	IMU+IR camera	✓	○	✓	×	–	–	–	–
Ours	–	–	RGB camera	✓	✓	✓	✓	2.9	3.2	97	10.4g

(e.g., EMG) or precise gesture classification (e.g., acoustic), but often trade off against noisy or ambiguous signals, environmental sensitivity, customized hardware, and coverage biased toward discrete poses rather than full 3D articulation.

Wrist-mounted optical systems leverage commodity cameras to get fine details of the fingers. RotoWrist estimates wrist orientation with surrounding IR modules [81]; WristCam observes the back-of-hand or environment for wrist trajectories [5]; FineType augments an under-wrist IR camera with IMU for tap detection [51]; multi-view wrist-mounted thermal imaging (FingerTrak) reconstructs full hand pose from hand silhouettes captured by four miniature thermal cameras on a wristband [27]. However, because distal fingertips and contacts are not directly observed in these setups, full-hand joint angles and the subtle appearance cues necessary for pressure inference (skin deformation, contact shadows, millimeter-scale fingertip displacements) remain under-captured.

WRISTP² mounts a fisheye RGB camera (180° FOV) on the palmar side of the wrist, providing a stable, body-anchored vantage that simultaneously exposes distal articulation and contact appearance. This enables continuous pose and pressure estimation in comfortable, hands-down postures, improves distal joint precision, and supports bare-hand interaction on uninstrumented surfaces without additional wearables. Notably, the wrist perspective directly observes fingertip skin deformation and contact shading—signals that are difficult to sustain from head-mounted viewpoints—thereby benefiting appearance-based pressure inference.

Taken together, existing placements present a trade-off: environment-mounted systems offer accuracy but limited mobility; head-mounted systems support mobility but suffer from FOV restrictions and "gorilla-arm" fatigue; and prior wrist-mounted systems lack the vantage point to capture contact mechanics. WRISTP² addresses these limitations by mounting a fisheye RGB camera on the palmar side of the wrist. This stable, body-anchored vantage directly

exposes distal articulation and fingertip skin deformation. This configuration enables continuous pose and pressure estimation in comfortable, hands-down postures, effectively unbinding interaction from the head’s field of view and the environment’s infrastructure.

3 Hardware Implementation

Our prototype system is primarily composed of a 180° FOV RGB camera module, a Raspberry Pi Zero 2 W, a nylon strap, and a custom 3D-printed enclosure, with a total hardware cost of approximately USD 50. While the electronic components and the strap are commercially available off-the-shelf, the enclosure was custom-designed to ensure wearing comfort and ergonomics.

As shown in Fig. 2, we designed a 3D-printed camera housing with a magnetized rotational hinge, enabling the camera to be quickly switched between a 90° working position and a 0° stowed position, minimizing the wearing burden when the device is not in use. The camera module is sized at 28 × 25 mm. The Raspberry Pi Zero 2 W and a 2000 mAh Li-Po battery are integrated into a compact 60 × 30 × 15 mm unit, enabling wireless image transmission and stable power supply within a small form factor.

For the data collection and user-study procedures described in Sections 4 and 7, a wired connection was employed to ensure real-time performance and transmission stability. In the real-world scenario evaluation presented in Section 8, we further validated a wireless version: images of 512 × 512 resolution at 30 fps were transmitted over a 2.4 GHz WLAN. The system operated continuously for approximately three hours under a maximum power consumption of about 1.5 W, demonstrating its practicality in everyday interaction scenarios.

Looking ahead, as illustrated in Fig. 2(d, e), we plan to integrate the camera and wireless communication module into a compact smartwatch form factor. By employing a high-integration SoC, a custom flexible PCB, and an optimized mechanical design, we envision two distinct hardware configurations.

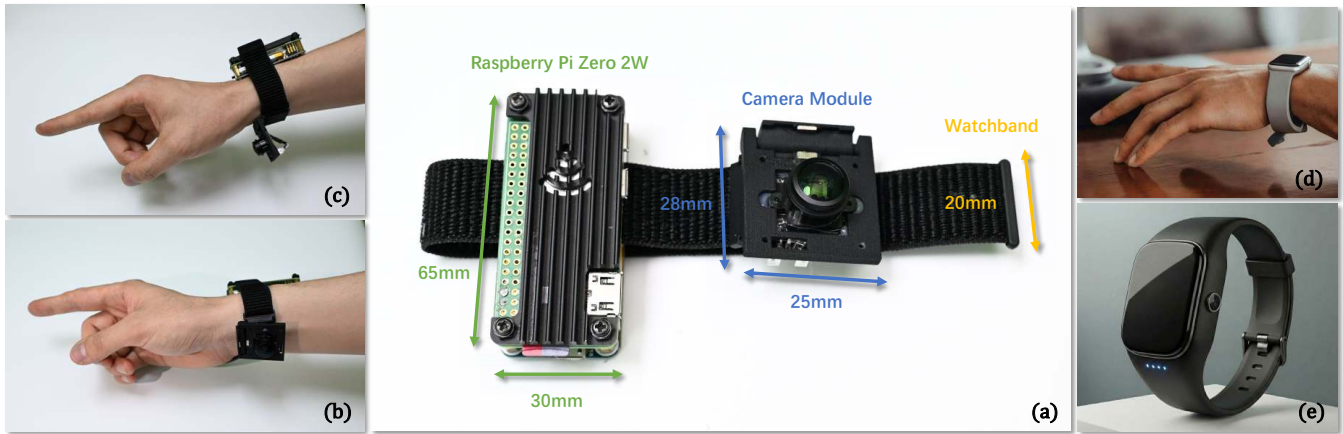


Figure 2: Hardware design of WRISTP². (a) System modules: right—180° FOV ultra-wide RGB camera module (28 × 25 mm), left—Raspberry Pi Zero 2 W with a battery-backed micro-UPS; (b) Stowed configuration worn on the wrist, with the overall thickness reduced to ≈ 10 mm for comfortable long-term wear; (c) In-use configuration with the camera deployed via a 90° magnetic fold-out hinge to provide a wrist-centric view from below the hand (height ≈ 28 mm); (d, e) Future integrated concept toward a smartwatch-style form factor.

The first design places the camera on the watch bezel or side. In daily use, the watch face remains dorsal (face-up); for interaction with VR headsets or other devices, users simply rotate the watch face toward the palmar side to activate WRISTP². This rotatable paradigm shares similarities with commercial devices like Omate TrueSmart and imoo [33, 72], which integrate side-mounted cameras.

The second design embeds the camera directly at the bottom of the watch chassis, enabling immediate interaction without mechanical rotation, a form factor successfully adopted by TapXR [103]. Both designs demonstrate the feasibility and strong commercial potential of wrist-worn optical sensing.

4 WRISTP² Dataset

4.1 Data Capture Setup

As shown in Fig. 3, to obtain high-fidelity annotations of hand pose and pressure, we designed a data collection system. The system integrates a sub-millimeter precision FZMotion MoCap system, a high-resolution pressure-sensitive touchpad (Sensel Morph) [86], a wrist-mounted camera, an Azure Kinect camera and a display terminal to guide user interactions. The Sensel Morph is placed horizontally on a tabletop to capture pressure distributions during hand-plane interactions. A wrist-mounted camera captures wrist-view images of hand, while a Kinect RGB camera mounted on a tripod captures third-person color images of global hand movements.

For a subset of participants, we additionally deployed a head-mounted RGB camera (as in Section 8.1) to capture synchronized egocentric views. While this dataset enables future multi-view fusion studies, here we use it solely to benchmark our wrist-based method against standard vision-based baselines. To ensure a fair

comparison, the head-mounted camera featured a 150° FOV, selected to maximize the field of view without introducing significant distortion. Details are provided in Appendix C.1.

We developed a data collection software with a user-friendly GUI that provides gesture videos and textual instructions, displays task timing and progress, and supports real-time monitoring, allowing the experimenter to promptly detect and address anomalies.

4.2 Data Capture Environment

To improve robustness and generalization, we randomized key environmental factors known to affect vision-based perception.

Lighting Diversity. We used fixed illumination fixtures that provided controllable lighting conditions. For each session, one of three illuminance levels—high, medium, or low—was randomly selected, where each level corresponded to a predefined range of illuminance (e.g., high: $I \in [500, 2000]$ lux; medium: $I \in [100, 500]$ lux; low: $I \in [1, 100]$ lux). This design ensured controlled yet stochastic variability across lighting conditions.

Background Control. Green screens were installed on three vertical sides and the base of the capture frame to stabilize the background and facilitate post-processing (e.g., hand segmentation and random background replacement).

Surface Texture Diversity. To model common desktop appearances, we prepared six textures: pure white, pure black, light wood grain, dark wood grain, light marble, and dark marble. For each participant, every recording session was conducted with a different texture, ensuring that all textures were covered across sessions. The assignment of textures to sessions was randomized and counterbalanced across participants to reduce ordering effects.

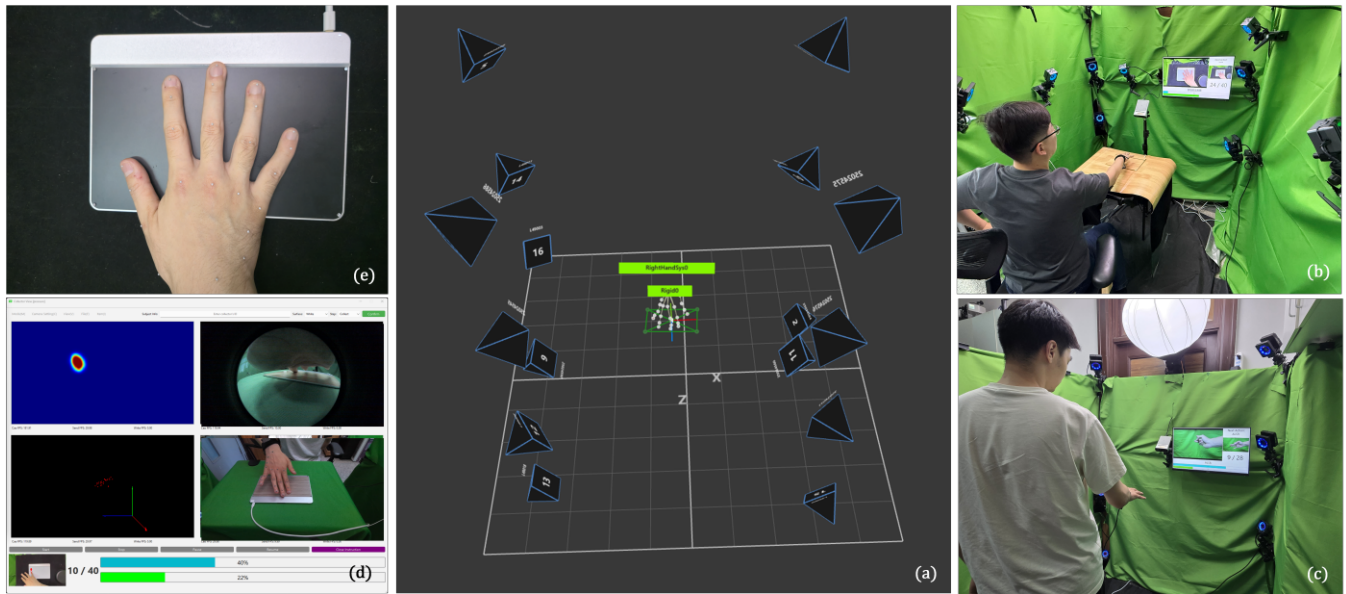


Figure 3: Collection Scene. (a) Visualization of the collection environment; (b) Planar interaction data collection; (c) Mid-air hand pose data collection; (d) The GUI of data collection software; (e) The 21 markers attached at the positions of the hand joint points and the 4 markers attached at the four corners of the Sensel Morph.

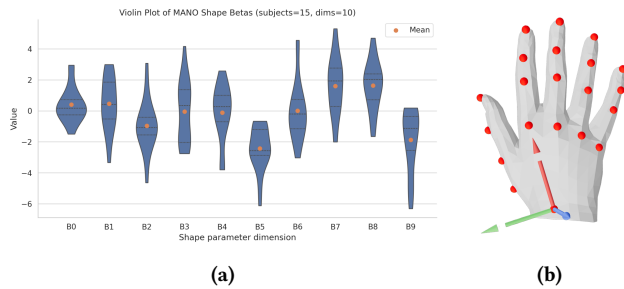


Figure 4: (a) Distribution of shape parameters β across participants. (b) Canonical hand-local coordinate system defined from anatomical markers.

4.3 Participants

We recruited 20 participants from our institution (15 male, 5 female; ages 19–28 years, $M = 24$). Among them, a subset of 5 participants additionally captured egocentric data using the head-mounted camera. The lengths of the middle finger ranged from 6.5 to 9.3 cm ($M = 7.1$, $SD = 0.48$), reflecting a diverse set of hand shapes within this demographic (see Fig. 4a for the distribution of MANO β values). We further categorized participants’ skin tones using the Fitzpatrick skin type scale (I–VI), which provides a standardized measure of skin pigmentation. The participants spanned Types II–IV, corresponding to light to medium skin tones typical among East Asian populations. Our current dataset does not cover the full spectrum of skin tones and demographics; extending to broader populations is an important direction for future work. Each participant who

successfully completed data collection received a compensation of \$15.

4.3.1 Preparatory Work. During preparation, participants were briefed on the tasks, provided informed consent, and viewed a demonstration video. We then placed 21 infrared-reflective markers on the dorsal joints of the right hand and affixed four markers to the corners of the Sensel Morph touchpad to delineate the pressure plane. Participants sat on adjustable stools and wore a wrist-mounted camera. Before data collection, they performed a calibration gesture by spreading their fingers and rotating their hand 3–4 times before the Kinect camera.

4.3.2 Planar Interaction Data Collection. The planar interaction data were collected in three sessions, with a different surface texture randomly selected from aforementioned six overlays for each session. These overlays represent common desktop surface finishes. Participants followed the sequential prompts on the screen to perform 48 actions, each lasting approximately 15 seconds. The actions covered common touchpad interactions—single- and multi-finger sliding, pressing, and pinching—as well as more complex behaviors such as symbol drawing, fingertip rotation, and rolling presses using different parts of the hand. Each session concluded with (i) a non-contact hover trial (fingers near but not touching the surface) to obtain data for non-contact conditions and (ii) a brief free-interaction segment without prompts. To simulate real-world use and introduce natural variation in fit and camera pose, participants removed and re-donned the wristband between consecutive sessions. A complete list and detailed definitions of these actions are provided in the Appendix A.

4.3.3 Mid-air Hand Pose Data Collection. Mid-air data were collected in two sessions. Across the sessions, participants performed a set of 28 gestures, each for approximately 15 seconds, including 10 American Sign Language (ASL) letters and common daily interaction gestures such as fist, OK sign, finger heart, grasping, pinching, pointing, rock gesture, thumbs-up, and claw pose. During these actions, participants were instructed to actively vary their wrist pitch and yaw angles to increase pose diversity. Each session ended with a short free-form movement segment to further enrich the dataset. As with the planar protocol, participants removed and re-donned the wristband between the two mid-air sessions to emulate realistic donning/doffing variability. Detailed descriptions of all gestures are provided in Appendix A.

4.3.4 Data Synchronization. Data collection from all sensors is triggered by a server, ensuring unified timebase. After correcting hardware delays, we aligned streams from high- to low-frame-rate devices, keeping the residual synchronization error within 5 ms. Additionally, participants are instructed to move smoothly to minimize synchronization errors.

An experimenter continuously monitored the recording interface and provided guidance. The total duration for each participant was approximately one hour, with breaks available on demand.

4.4 Annotation Method

To obtain high-fidelity hand meshes and per-vertex pressure from raw measurements, we develop a marker-based, multi-objective optimization pipeline built on the MANO model [80] (overview in Fig. 5). Given (i) 21 infrared-reflective markers stuck on the hand in the world frame, (ii) synchronized third-person RGB images, and (iii) calibrated pressure frames from a Sensel Morph touchpad, the pipeline fuses these observations to jointly estimate pose, shape, extrinsics, and a per-vertex pressure field. All quantities are formulated in a canonical hand-local coordinate system that we define algorithmically from anatomical landmarks (Sec. 4.4.1); accordingly, we estimate the rigid transformation between the world frame and the hand-local frame.

4.4.1 Hand-Local Canonical Coordinate System. To provide a consistent reference frame across participants and sessions, we introduce a hand-local canonical coordinate system, which serves as the basis for both annotation optimization and network prediction. This local frame is defined algorithmically from anatomical markers on the hand mesh. Performing optimization and prediction in this canonical hand-local frame removes global translation and rotation degrees of freedom, improving numerical stability and convergence. An illustration of this coordinate system is provided in Fig. 4b, while its detailed definition is described in the supplementary material.

Initialization. We follow the approach of [40] to obtain the shape parameter β , which is fixed during subsequent optimization. The initial MANO pose θ_{init} is predicted by a graph neural network pre-trained on our self-collected large-scale dataset 5.2.1. This network takes as input the 3D coordinates of 21 fixed mesh vertices in the canonical hand-local frame, on the hand mesh, and outputs the MANO pose parameters. The same dataset is also used to train our

Hand-VQ-VAE to provide a strong prior knowledge of hand geometry; details of the dataset construction and statistics are provided in supplementary.

For extrinsics, the initial rigid transformation is obtained from markers (denoted by $[R_L^{(0)W} | T_L^{(0)W}]$ or its inverse), but due to calibration noise it is not treated as ground truth. Therefore, in optimization we refine extrinsics *per frame* via incremental updates:

$$R_L^W = R_L^{(0)W} \Delta R, \quad T_L^W = T_L^{(0)W} + \Delta T,$$

where $(\Delta R, \Delta T)$ are the learnable deltas.

4.4.2 Annotation Optimization. The hand mesh in the hand-local coordinate system is written as $\mathcal{V}_l = \text{MANO}(\theta, \beta^*)$, and the world-space vertices are

$$\mathcal{V}_w = R_L^W \mathcal{V}_l + T_L^W = (R_L^{(0)W} \Delta R) \mathcal{V}_l + (T_L^{(0)W} + \Delta T).$$

We optimize

$$\Theta = \{\theta, \Delta R, \Delta T, \mathcal{P}_v\} \quad (\beta \text{ fixed to } \beta^*)$$

by minimizing

$$\mathcal{L}_{\text{opti}}(\Theta) = \mathcal{L}_{\text{markers}}(\Theta) + \mathcal{L}_{\text{mask}}(\Theta) + \mathcal{L}_{\text{render}}(\Theta) + \mathcal{L}_{\text{anat}}(\Theta). \quad (1)$$

Orthographic camera and differentiable rendering. We use a virtual orthographic camera placed beneath the center of the Sensel Morph plane and looking upward along the plane normal. The camera resolution matches the sensor grid ($H \times W$). Two render passes are computed with a differentiable renderer: a *pressure* pass and a *depth* pass. For the pressure pass, the per-vertex pressure \mathcal{P}_v is assigned as the surface texture of \mathcal{V}_w , yielding a rendered pressure map $\tilde{\mathcal{R}}_p$. After a vertical flip to align the sensor convention, we penalize the pixel-wise MSE to the ground-truth pressure map P_{gt} . For the depth pass, we render a depth map $\tilde{\mathcal{R}}_d$ and convert it to the *relative-to-plane depth* by subtracting a calibrated offset $\delta = 0.1$: $d_{\text{rel}} = \tilde{\mathcal{R}}_d - \delta$. We then produce a soft contact probability $\hat{C} = \sigma((\epsilon - d_{\text{rel}})/\tau)$ and apply a BCE-with-logits loss against the binary contact mask $M_{\text{contact}} = \mathbf{1}_{\{P_{\text{gt}} > \gamma\}}$ within the projected hand region M_{hand} .

Rendering losses. We therefore write

$$\mathcal{L}_{\text{render}}(\Theta) = \omega_{\text{press}} \mathcal{L}_{\text{press}}(\text{Flip}(\tilde{\mathcal{R}}_p), P_{\text{gt}}) + \omega_{\text{hand}} \mathcal{L}_{\text{hand}}. \quad (2)$$

with:

$$\mathcal{L}_{\text{press}} = \frac{1}{HW} \|\tilde{\mathcal{R}}_p - P_{\text{gt}}\|_F^2, \quad (3a)$$

$$\mathcal{L}_{\text{hand}} = \frac{1}{\|M_{\text{hand}}\|_1} \left\| M_{\text{hand}} \odot \ell\left(\frac{\epsilon - (\tilde{\mathcal{R}}_d - \delta)}{\tau}, M_{\text{contact}}\right) \right\|_1. \quad (3b)$$

Here, $\text{Flip}(\cdot)$ denotes a vertical flip to match the sensor's raster order, $\sigma(\cdot)$ is the logistic function and $\ell(\cdot, \cdot)$ denotes the element-wise BCE-with-logits. M_{hand} is the projected hand mask, and $M_{\text{contact}} = \mathbf{1}_{\{P_{\text{gt}} > \gamma\}}$ is the binary contact mask.

Anatomical loss. The anatomical loss $\mathcal{L}_{\text{anat}}$ regularizes the pose parameters to ensure biologically plausible hand configurations [112]. This discourages physically implausible finger bending, twisting, spreading, and improves the stability of the optimization.

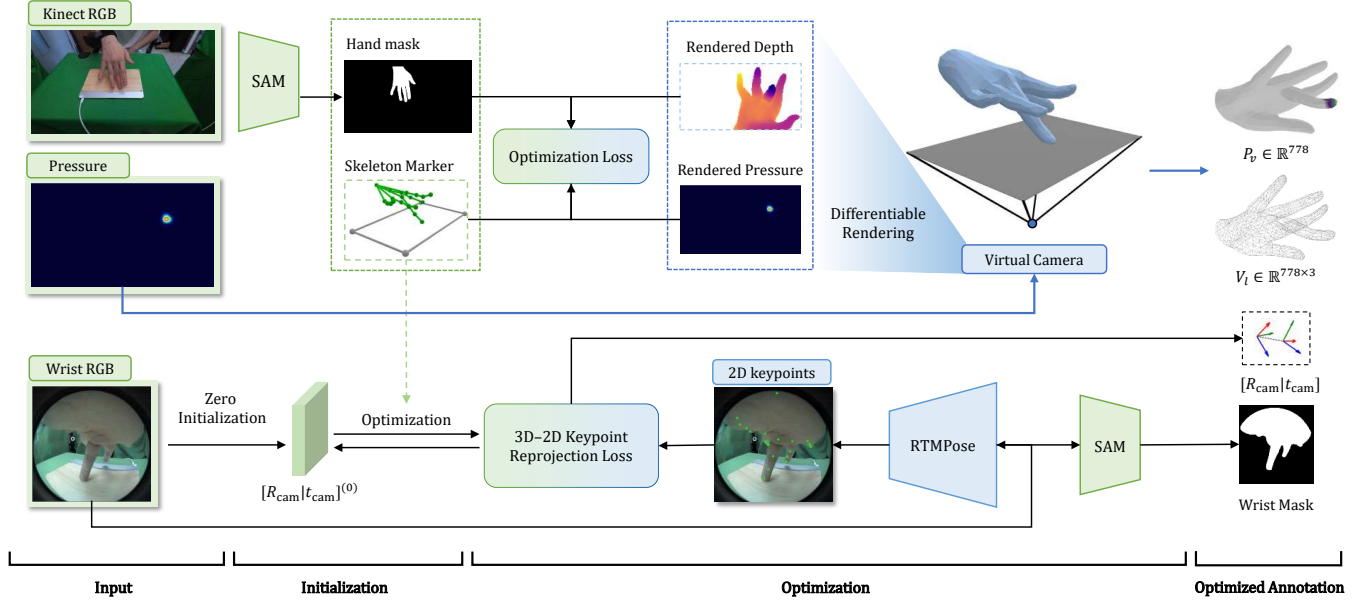


Figure 5: Annotation pipeline overview. The pipeline consists of two parallel stages to generate ground-truth data. **Top (Hand & Pressure Optimization):** We fuse multi-modal inputs—including third-person Kinect RGB images, motion-capture markers, and tactile pressure maps—to jointly optimize the hand mesh geometry V_i and the per-vertex pressure field P_v . A differentiable rendering module minimizes the discrepancy between simulated and observed pressure/depth maps. **Bottom (Wrist Camera Calibration):** Using the reconstructed 3D hand as a reference, we estimate the wrist camera extrinsics $[R_{cam}|t_{cam}]$ relative to the hand-local frame. This is achieved by minimizing the 3D-2D reprojection loss between the projected 3D joints and 2D keypoints detected by RTMPose from the raw wrist-camera inputs.

Intuition. This design serves two purposes: (i) it constrains the predicted 2D pressure projection to match the ground-truth sensor map, and (ii) it encourages the *contact foreground* to lie close to the plane while pushing the *background* away from it, while the per-frame extrinsic deltas $(\Delta R, \Delta T)$ compensate for calibration bias in the marker-derived initialization.

4.4.3 Wrist-mounted Camera Extrinsic Annotation. To annotate the extrinsics of the wrist-mounted camera, we adopt a 2D–3D joint alignment approach. Specifically, we randomly sampled 3000 images from the wrist-mounted camera stream and manually annotated the 2D positions of 21 hand joints in each image. A 2D joint detection model was then trained within the MMPose [85] framework by finetuning the RTMPose model [38], achieving an MPJPE of 6.2 pixels on the held-out test set at 512×512 resolution. This model was used to produce 2D joint annotations for the entire dataset.

For extrinsic calibration, we employ the ocamcalib polynomial fisheye camera model [84] to project the ground-truth 3D joints onto the image plane using the pre-calibrated intrinsics. The camera extrinsics $[R_{cam}|t_{cam}]$ are then estimated by solving the following least-squares optimization problem:

$$\min_{R_{cam} \in \text{SO}(3), t_{cam} \in \mathbb{R}^3} \sum_{i=1}^N \left\| \pi_{\text{ocam}}(R_{cam} X_i + t_{cam}) - u_i \right\|_2^2, \quad (4)$$

where X_i are the 3D joints in the hand-local frame, u_i are the detected 2D joint coordinates, and $\pi_{\text{ocam}}(\cdot)$ denotes the ocamcalib

projection function. It is important to note that these extrinsics are defined with respect to the hand-local coordinate system introduced in Sec. 4.4.1, ensuring consistency with our annotation pipeline.

5 WRISTP² Algorithm

5.1 Model Architecture

Overview. WRISTP² jointly predicts (i) the canonical hand mesh, (ii) per-vertex contact and pressure, and (iii) the wrist-mounted camera extrinsics. A shared ViT-based backbone produces patch embeddings. From these features, two *joint-aligned* token sets (21 tokens each, aligned to anatomical joints) query the backbone features tokens via cross-attention for pose and pressure regression. In parallel, a lightweight regression branch predicts the wrist-camera extrinsics in the hand-local frame from raw RGB image; the predicted extrinsics are embedded and concatenated to both token sets before cross-attention, ensuring that token interactions are conditioned on viewpoint geometry.

For the pose pathway, each cross-attended *pose token* independently solves a classification problem over the Hand-VQ-VAE. The resulting discrete indices are used to retrieve the corresponding codebook embeddings, which are fed into the Hand-VQ-VAE decoder to obtain MANO parameters (θ, β) ; the MANO layer then maps (θ, β) to mesh vertices, reconstructing the canonical hand mesh. In contrast, the 21 pressure tokens are globally pooled into a single embedding that is mapped to two 778-dimensional outputs: a

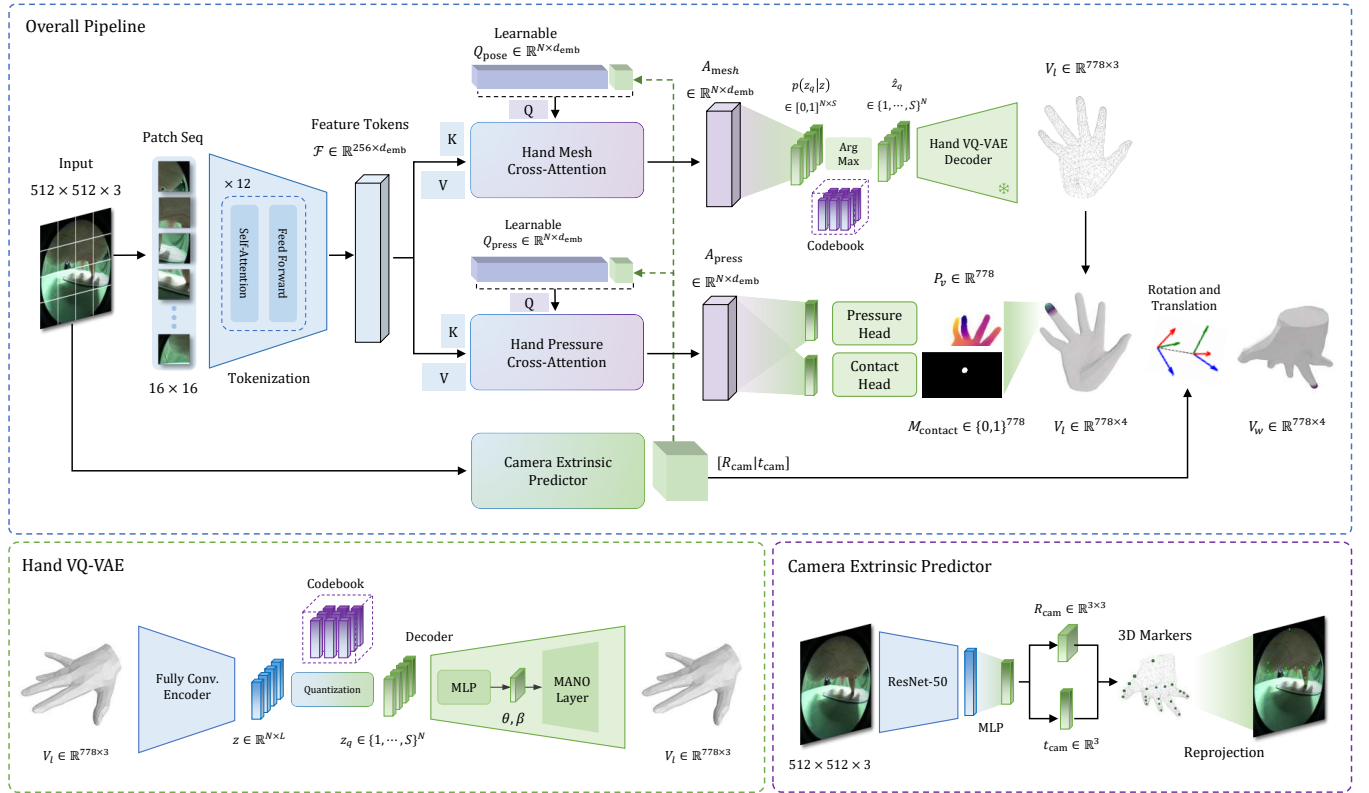


Figure 6: WRISTP² pipeline. A ViT-based backbone produces image features that are queried by two sets of learnable tokens (pose- and pressure-tokens, both of length 21). The wrist-camera extrinsics are embedded and *concatenated channel-wise to both token sets before cross-attention*, yielding extrinsics-aware token features. The pooled token features are fed into task-specific heads: a codebook indices classification head (decoded by Hand-VQ-VAE decoder), and a *pressure branch with two heads* for contact classification and pressure regression.

contact classification head (per-vertex contact logits) and a pressure regression head (per-vertex pressure magnitudes).

5.1.1 Canonical Hand Mesh Tokenization. Vector-Quantized VAE (VQ-VAE)[105] is a discrete representation learning technique originally developed for image generation. Recent studies[14, 16, 17] show its strong performance in pose estimation and mesh reconstruction, especially under limited data size. Following them, we adopt a variant of Mesh-VQ-VAE[119] whose encoder is a Fully convolutional mesh autoencoder, while the decoder is replaced by a MLP followed by a MANO layer. We denote it Hand-VQ-VAE. This design tokenizes the canonical hand mesh into latent representation space, thus making the mesh reconstruction problem into a simple classification problem. In Hand-VQ-VAE, the codebook comprises 512 embedding vectors in \mathbb{R}^9 . For each input frame, the encoder produces 21 latent vectors, which are quantized via nearest-neighbor lookup in the 512-way codebook, yielding 21 code indices.

5.1.2 Pressure Branch. The 21 extrinsics-aware *pressure tokens* are globally pooled into a fixed-length vector \bar{t}_{press} :

$$\bar{t}_{\text{press}} = \text{Pool}(T_{\text{press}}) \in \mathbb{R}^{d_{\text{emb}}}.$$

From this embedding, two parallel heads produce per-vertex predictions: (i) a **contact classification head**, outputting logits $m \in \mathbb{R}^{778}$ (after sigmoid to obtain contact probabilities), and (ii) a **pressure regression head**, outputting $p \in \mathbb{R}^{778}$ as continuous pressure values. We simply use a pressure threshold to generate gt contact mask.

This decoupled design is particularly beneficial under the foreground-sparsity regime, where only a small subset of hand vertices are in contact while the majority are background. By letting the contact head explicitly address the highly imbalanced classification problem (with focal-style supervision), and conditioning pressure regression on the detected foreground, the model suppresses background leakage and stabilizes training, leading to more reliable pressure estimation in sparse-contact scenarios.

5.1.3 Pose Branch. The 21 extrinsics-aware *pose tokens* are aligned to anatomical joints. Each token independently solves a classification problem over the Hand-VQ-VAE codebook:

$$P(z_q | z) \in [0, 1]^{21 \times S},$$

where S is the codebook size. The predicted discrete indices are used to retrieve the corresponding codebook embeddings, which are then passed through the Hand-VQ-VAE decoder to obtain MANO parameters (θ, β) . Finally, a differentiable MANO layer maps these

parameters to the mesh vertices

$$V_H = \text{MANO}(\theta, \beta) \in \mathbb{R}^{778 \times 3},$$

reconstructing the canonical hand mesh. Thanks to the asymmetric encoder–decoder design of Hand–VQ–VAE, the shape parameter β can be fixed during inference. This reduces inter-frame drift and suppresses spurious variations, which is crucial for identity consistency in interactive use.

5.1.4 Camera Extrinsic Branch. A lightweight predictor regresses the wrist-mounted camera extrinsics relative to the hand-local frame $\{H\}$. Instead of directly predicting absolute camera extrinsics, we let the network estimate a *delta* with respect to the dataset-averaged extrinsics, which empirically stabilizes optimization. Concretely, a ResNet-50 backbone (initialized from ImageNet pretraining) extracts image features that are fed into a small MLP head. The branch outputs a 6D rotation representation $\Delta \mathbf{r}_{6D} \in \mathbb{R}^6$ and a translation offset $\Delta t_{\text{cam}} \in \mathbb{R}^3$. These deltas are composed with the dataset mean extrinsics $(\bar{R}_{\text{cam}}, \bar{t}_{\text{cam}})$ to yield

$$\hat{R}_{\text{cam}} = \exp([\Delta\omega]_{\times}) \bar{R}_{\text{cam}}, \quad \hat{t}_{\text{cam}} = \bar{t}_{\text{cam}} + \Delta t_{\text{cam}},$$

where $\Delta\omega$ is the axis–angle vector converted from $\Delta \mathbf{r}_{6D}$ by orthonormalization [118]. Finally, the embedding e_{cam} is replicated and concatenated to both pose and pressure token sets before cross-attention:

$$\tilde{Q}_{\text{pose}} = [Q_{\text{pose}}; E_{\text{cam}}], \quad \tilde{Q}_{\text{press}} = [Q_{\text{press}}; E_{\text{cam}}],$$

making both branches explicitly conditioned on viewpoint geometry.

5.2 Model Training

5.2.1 Hand–VQ–VAE. We pretrain Hand–VQ–VAE on public datasets (Gigahand [18], HO3D [23], Interhand [67], HanCo [120], DexYCB [3], FreiHand [122]) after transforming meshes to the hand-local frame, and then finetune on our dataset, achieving 2.1 mm per-vertex reconstruction error.

5.2.2 Data Augmentation. We apply random background replacement tailored to wrist-mounted fisheye imagery. First, we segment the hand with SAM2 to obtain a binary mask. Then, panoramas from an indoor dataset [110] are warped to the fisheye image plane using the pre-calibrated intrinsics \mathbf{K}_{fish} [84] and a pose sampled from $\text{SE}(3)$. During training, we replace the background with probability 0.5. Representative visualizations of this background replacement are shown in Fig. 7; algorithmic details are provided in the supplementary material.

For both the replaced-background samples and pose-only samples, we manually set pressure labels to zero. Standard photometric augmentations are also applied: illumination jitter, random gamma, and additive noise.

5.2.3 Loss Function. Let $\hat{R}_{\text{cam}}, \hat{t}_{\text{cam}}$ be predicted extrinsics; $R_{\text{cam}}^*, t_{\text{cam}}^*$ ground truth. Let $J \in \mathbb{R}^{K \times 3}$ denote 3D joints in $\{H\}$ and $\pi(\cdot)$ denote projection under fisheye intrinsics.

(1) *Extrinsic loss with residualization.* We predict a residual $\Delta\xi = (\Delta\omega, \Delta t)$ and compose it with a running estimate (R_0, t_0) :

$$\hat{R}_{\text{cam}} = \exp([\Delta\omega]_{\times}) R_0, \quad \hat{t}_{\text{cam}} = t_0 + \Delta t.$$

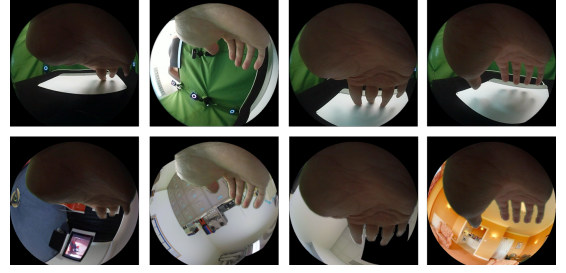


Figure 7: Example of the wrist-mounted camera image with random replaced background

The loss combines 2D keypoint reprojection and direct pose terms:

$$\begin{aligned} \mathcal{L}_{\text{ext}} = & \lambda_{\text{kp}} \frac{1}{K} \sum_{k=1}^K \|\pi(\hat{R}_{\text{cam}} J_k + \hat{t}_{\text{cam}}) - u_k^*\|_1 \\ & + \lambda_R d_{\text{geo}}(\hat{R}_{\text{cam}}, R_{\text{cam}}^*) + \lambda_t \|\hat{t}_{\text{cam}} - t_{\text{cam}}^*\|_1. \end{aligned}$$

where $d_{\text{geo}}(R_1, R_2) = \|\log(R_2^T R_1)\|_2$ is the geodesic distance on $\text{SO}(3)$. Residualization (predicting $\Delta\xi$) empirically stabilizes training.

(2) *VQ-VAE index loss.* For $N=21$ tokens and codebook size $S=512$, we use token-wise cross-entropy:

$$\mathcal{L}_{\text{vq}} = \frac{1}{N} \sum_{n=1}^N \text{CE}(\hat{\mathbf{p}}_n, q_n^*), \quad \hat{\mathbf{p}}_n \in \mathbb{R}^S.$$

(3) *Pressure and contact losses.* Let contact logits be $m \in \mathbb{R}^{778}$, pressure prediction $p \in \mathbb{R}^{778}$, and ground-truth pressure $\mathbf{p}^* \in \mathbb{R}^{778}$ (with zeros on replaced/pure-pose samples). Define positive-contact mask $\mathbf{c}^* = \mathbf{1}(\mathbf{p}^* \cdot h_{\text{max}} > \tau)$ with scale h_{max} and threshold τ . We use focal loss for contact:

$$\mathcal{L}_{\text{contact}} = \text{FocalBCE}(m, \mathbf{c}^*; \alpha, \gamma).$$

For pressure regression we apply a soft gate $g = \sigma(m)$ and enforce non-negativity of predictions using *softplus*:

$$\tilde{p} = (g^{\text{gate}}) \cdot \text{softplus}(p).$$

Foreground/background are split by \mathbf{c}^* :

$$\mathcal{L}_{\text{press}} = \frac{1}{|\text{FG}|} \sum_{v \in \text{FG}} (\tilde{p}_v - \mathbf{p}_v^*)^2 + \lambda_{\text{bg}} \frac{1}{|\text{BG}|} \sum_{v \in \text{BG}} |\tilde{p}_v|.$$

The overall pressure loss is

$$\mathcal{L}_{\text{prs}} = \mathcal{L}_{\text{contact}} + \mathcal{L}_{\text{press}}.$$

(4) *Total loss.*

$$\mathcal{L} = \lambda_{\text{ext}} \mathcal{L}_{\text{ext}} + \lambda_{\text{vq}} \mathcal{L}_{\text{vq}} + \lambda_{\text{prs}} \mathcal{L}_{\text{prs}}.$$

5.2.4 Training Setting. The experiment was conducted on six RTX 4090 GPUs, with a total training time of approximately six hours. We used the AdamW optimizer with a learning rate of 1×10^{-5} and a global batch size of 32. The learning rate followed a OneCycle schedule.

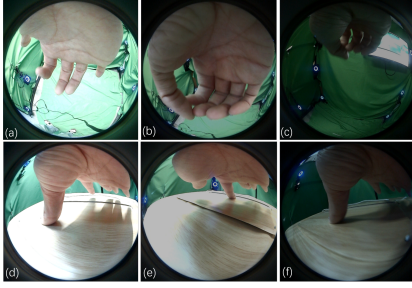


Figure 8: Example wrist-camera views under different illumination conditions. Top row: mid-air hand poses; bottom row: planar interaction on the surface. From left to right: high, medium, and low illumination.

Table 2: Pose accuracy across illumination conditions. Position errors in mm; MJAE in degrees ($^{\circ}$). Lower is better.

Illumination	MPJPE	PA-MPJPE	PVE	PA-PVE	MJAE [$^{\circ}$]
High (H)	2.7	2.3	2.8	2.5	3.0
Medium (M)	2.8	2.4	2.9	2.6	3.1
Low (L)	3.1	2.7	3.2	2.9	3.3
All	2.9	2.4	3.0	2.6	3.2

6 Offline Evaluation

We evaluate WRISTP² on three core tasks: (i) 3D hand pose reconstruction, (ii) per-vertex pressure estimation, and (iii) wrist-camera extrinsics estimation. Beyond reporting overall performance, we explicitly analyze the system’s robustness to two critical factors: environmental illumination and wrist orientation. First, we report results across three illumination levels I : High (H, $2000 \geq I \geq 500$ lux), Medium (M, $100 \leq I < 500$ lux), and Low (L, $I < 100$ lux), as visualized in Figure 8. Second, we investigate the impact of wrist orientation on reconstruction accuracy to validate the effectiveness of our camera design in handling extreme viewpoints. In addition, we compare WRISTP² against several existing methods for 3D hand pose reconstruction and pressure estimation under all these different settings. Due to space constraints, the full experimental setup and comparison details is reported in Appendix C.1.

6.1 Pose Reconstruction

We first evaluate the accuracy of 3D hand pose reconstruction in the hand-local frame. We use standard metrics: MPJPE (Mean Per-Joint Position Error), PA-MPJPE (Procrustes-Aligned Mean Per-Joint Position Error), PVE (Per-Vertex Error), PA-PVE, and MJAE (Mean Joint Angle Error). Table 2 summarizes the results.

WRISTP² achieves high accuracy with an overall MPJPE of 2.9 mm and MJAE of 3.2° . Notably, the system demonstrates strong robustness to illumination changes. As lighting conditions degrade from High to Low, the error increase is marginal (e.g., MPJPE increases by 0.4 mm).

Table 3: Contact and pressure accuracy across surfaces. IoU $\in [0, 1]$ and Contact Accuracy in % (higher is better). MAE in gram-force (g; lower is better).

Surface	Cont. IoU	Vol. IoU	Cont. Acc. (%)	MAE _{FG}	MAE _{ALL}
Light Wood	0.723	0.624	97.5	9.7	0.107
Dark Wood	0.716	0.618	94.8	10.2	0.108
Light Marble	0.679	0.606	96.2	11.8	0.122
Dark Marble	0.673	0.591	95.5	12.4	0.127
Black	0.703	0.610	95.4	10.8	0.118
White	0.730	0.631	98.1	9.2	0.104
All	0.712	0.618	97.1	10.4	0.111

Table 4: Contact and pressure accuracy under different illumination conditions. IoU $\in [0, 1]$ and Contact Accuracy in % (higher is better). MAE in gram-force (g; lower is better).

Illumination	Cont. IoU	Vol. IoU	Cont. Acc. (%)	MAE _{FG}	MAE _{ALL}
High (H)	0.730	0.635	98.9	9.7	0.102
Medium (M)	0.712	0.614	97.4	10.4	0.109
Low (L)	0.690	0.600	96.1	11.1	0.120
All	0.712	0.618	97.1	10.4	0.111

6.2 Pressure Estimation

Next, we evaluate per-vertex contact and pressure estimation. Metrics include Contact IoU (Contact Intersection over Union), Vol. IoU (Volumetric Intersection over Union), Contact Accuracy (threshold >10 g), and MAE (Mean Absolute Error) for foreground (MAE_{FG}) and all vertices (MAE_{ALL}). Table 3 and Table 4 detail the performance across different surfaces and lighting conditions.

The system maintains high reliability across different surface textures, as shown in Table 3. Clean and bright textures yield optimal results; for instance, the White surface achieves the lowest MAE_{FG} of 9.2 g. While complex textures like Dark Marble present a challenge, increasing MAE_{FG} to 12.4 g. Notably, the Contact Accuracy remains consistently above 90% across all surfaces. This suggests that our network successfully learns to decouple geometric deformation cues from textural noise, ensuring reliable contact detection even on visually challenging surfaces.

Similarly, the system demonstrates resilience to illumination changes (Table 4). Performance is stable between High and Medium settings, with MAE_{ALL} increasing marginally. Although Low-light conditions inevitably reduce the Signal-to-Noise Ratio (SNR), leading to a drop in Contact IoU to 0.690, the performance remains at a usable level, indicating that our proximal wrist-camera setup captures sufficient close-range visual features to support continuous interaction, preventing the complete failure often seen in environment-based systems under dim lighting.

6.3 Wrist-Camera Extrinsics Estimation

Finally, we analyze the camera extrinsics prediction capability of WRISTP². Table 5 reports the results. The system achieves precise

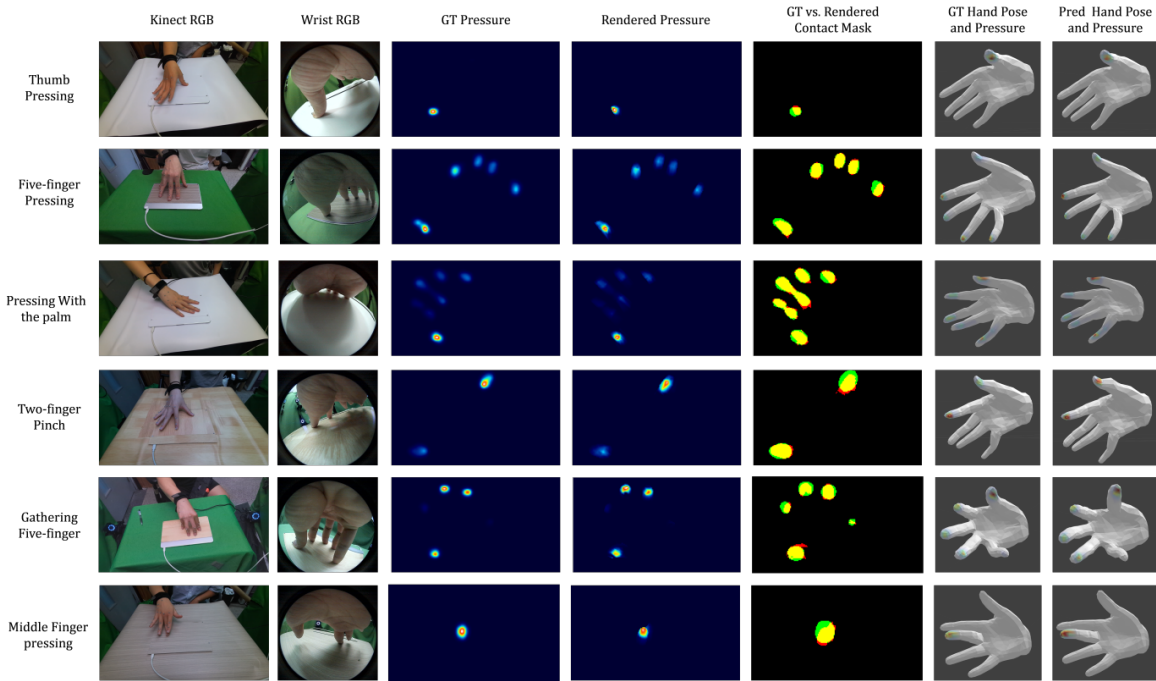


Figure 9: Qualitative results of planar interaction. The fifth column compares Ground Truth (Red) and Prediction (Green), with Yellow indicating overlap.

Table 5: Wrist-camera extrinsics accuracy across illumination conditions. Rotation in degrees ($^{\circ}$), translation in mm, reprojection in px. All metrics lower is better.

Illum.	Rot. Err. ($^{\circ}$)	Trans. Err. (mm)	2D Reproj. (px)
High (H)	2.1	8.5	13.1
Medium (M)	2.3	9.0	13.8
Low (L)	2.4	9.3	14.4
All	2.3	8.9	13.7

extrinsics estimation with a rotation error of 2.3° and translation error of 8.9 mm.

Impact of Wrist Orientation. The pitch angle determines the proportion of the hand in the camera frame. A larger proportion provides more visual details but may introduce near-field distortion, while a smaller proportion reduces the effective resolution. We analyze the MPJPE w.r.t wrist pitch angle in Figure 10.

As illustrated in Figure 10, although the error distribution correlates with wrist orientation, the system maintains high accuracy within the most densely populated angular ranges. Figure 11 presents representative examples across these ranges to illustrate the system’s robustness:

- In the canonical range (-30° to 0°), the hand is centered with an optimal proportion. For the sample shown in Fig. 11b (-15.1°), the system yields a low MPJPE of ≈ 2.9 mm.

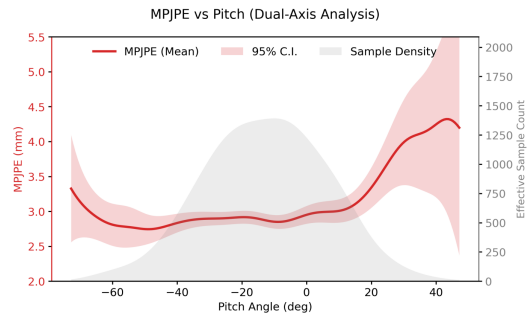


Figure 10: Error analysis w.r.t wrist pitch angle. The red curve shows the MPJPE (mean with 95% confidence interval). While error is minimized in the canonical range, the system maintains stable performance (sub-4.5 mm error) even at extreme angles, demonstrating the robustness of the fisheye design.

- At extreme negative angles (e.g., -60°), the hand occupies a large proportion of the frame. Although perspective distortion increases, the specific case in Fig. 11a (-61.2°) shows an error of ≈ 3.3 mm, verifying that the fisheye lens effectively captures sufficient detail even under severe distortion.
- At positive extremes ($> 30^{\circ}$), the hand recedes to the periphery, reducing its proportion in the frame. While this generally challenges the algorithm, the example in Fig. 11c (35.4°) demonstrates functional accuracy with an MPJPE of

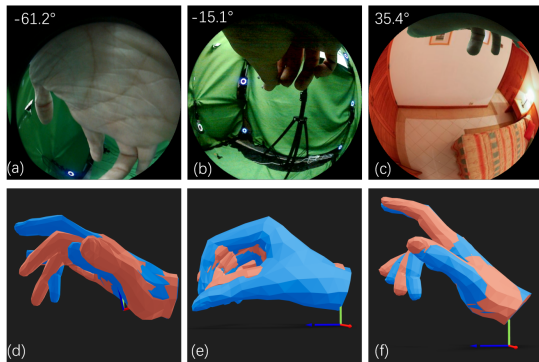


Figure 11: Qualitative visualization across pitch angles. The top row displays raw fisheye inputs, while the bottom row shows the corresponding 3D mesh reconstructions in the camera coordinate system. Legend: The **Blue** mesh represents Ground Truth (GT), and the **Red** mesh represents the Prediction. The coordinate triad at the origin marks the camera center, where the blue axis indicates the Z-axis (camera viewing direction). (a, d) **Extreme Negative Pitch** (-61.2°): The hand occupies a significant portion of the frame with strong fisheye distortion. (b, e) **Canonical Range** (-15.1°): The hand is centered with optimal scale and visibility. (c, f) **Extreme Positive Pitch** (35.4°): The hand recedes to the periphery, yet the system maintains robust tracking.

≈ 4.3 mm, confirming that the wide Field-of-View prevents tracking loss.

We refer to Appendix D for additional visualization results of pose prediction under varying wrist pitch angles.

In conclusion, WRISTP² delivers relatively consistent performance across varying illumination, surfaces, and wrist orientations. Our pitch-sweep analysis indicates that WRISTP² maintain high accuracy around the canonical wrist angles. In practice, this suggests that a palm-facing fisheye camera mounted near the wrist can robustly accommodate natural hand postures, while interactions that require fully pronated or supinated forearms remain challenging. These findings provide guidance on where wrist-mounted vision is best suited and where additional sensing (e.g., head-mounted or non-visual modalities) may be needed.

7 USER STUDY

To systematically evaluate the performance of WRISTP² for both on-plane and mid-air interaction, we conducted three user studies: (1) mid-air cursor control; (2) multi-finger pressure input on a desktop surface; and (3) a composite virtual pressure-sensitive touchpad task integrating both fingertip displacement and pressure cues.

To ensure stable data collection and consistent evaluation, all three studies used a wired data transmission setup. Dedicated GUIs were developed for each task. We further randomized lighting conditions and surface textures following the same protocol as in the dataset collection phase (Section 4). The experimental setups for these studies are illustrated in Fig. 12.

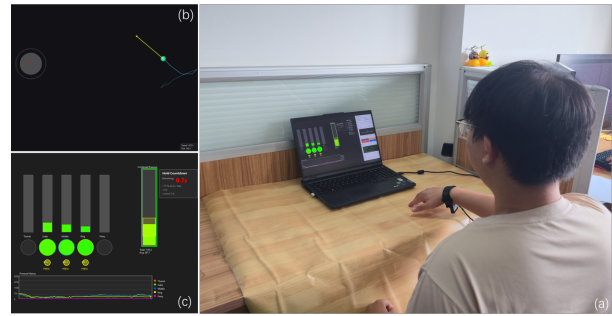


Figure 12: Experimental setup for the first three user studies. All studies were conducted in the same environment (a), under varying light conditions and surface textures. User Studies 1 and 3 employed the GUI shown in (b), while User Study 2 used the GUI in (c).

7.1 Participants

A total of 18 right-handed participants (3 females, aged 20–25, $M = 24.0$) from our institution took part in the studies consecutively after a 5-minute tutorial and a brief familiarization period. All participants were familiar with conventional mice and touchpads, but none had prior experience with the WRISTP² system.

7.2 Apparatus

All Python-based applications for User Studies 1-3 were executed on a Lenovo Legion Y9000P laptop equipped with an Intel Core i9-13900HX processor (13th Gen, 2.2 GHz), 16 GB of RAM (5600 MT/s), and an NVIDIA GeForce RTX 4060 Laptop GPU (8 GB VRAM). The system was running Windows 11 Home (64-bit, version 24H2). In the Virtual Air Mouse study (Study 1), we additionally included two conventional input devices as baselines: the laptop’s built-in touchpad and a Lenovo LEGION M500 RGB gaming mouse.

7.3 USER STUDY 1: Mid-Air Cursor Control

7.3.1 Design and Procedure. The first study evaluated the system’s capability to estimate hand postures to accomplish precise cursor movements. In this study, the participants’ index finger served as a virtual air mouse to control the cursor in a Fitts’ Law experiment. The index-finger coordinates (x , y) in the hand-local coordinate system were linearly mapped to the computer mouse coordinates on the screen using scaling factors of 23,000.0 (x direction) and 11,000.0 (y direction). We computed the Euclidean distance between the thumb and the index finger. When the distance was smaller than the contact threshold (5 mm), the virtual air mouse was recognized as a press, thereby enabling click and long-press functions similar to those of conventional input devices.

In each trial, a green button and a gray circular target were generated at random locations on the screen. The green button had a fixed diameter of 10 mm, whereas the diameter of the gray target varied from 30 mm to 90 mm. The center-to-center distances ranged from 40 mm to 400 mm, and initial positions were constrained to preclude spatial overlap. Participants initiated each trial by long-pressing the green button. Timing began when they started moving the button and stopped once it had been dragged into the gray

circular target and held there for 250 ms. Each participant completed 50 trials for each input device (virtual air mouse, touchpad, and mouse). After every block of 10 trials, a 2-minute rest interval was provided, during which participants were required to remove the wristband.

7.3.2 Measures and Analysis. For each trial, the diameter of the gray circular target, the initial center-to-center distance between the green button and the gray target, and the trial completion time were recorded.

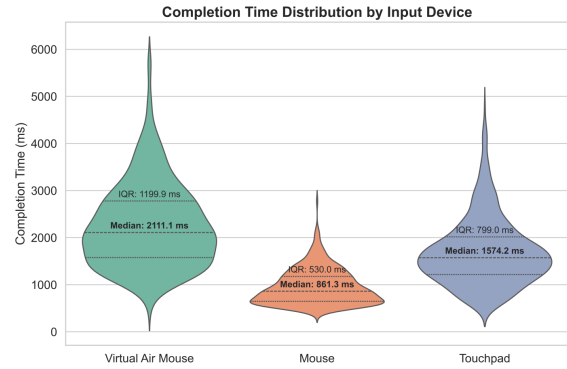
7.3.3 Results. To assess the significance of differences in task performance among the three input modalities, we conducted Friedman tests (as the data did not meet normality assumptions). The Friedman test results indicated a significant difference in the median completion times across the three input methods ($\chi^2 = 41.05, p < 0.001$). The mouse (Median = 861.3 ms, IQR = 530.0 ms) demonstrated superior selection speed, with both the touchpad (Median = 1574.2 ms, IQR = 799.0 ms) and the virtual air mouse (Median = 2111.1 ms, IQR = 1199.9 ms) showing significantly lower performance relative to the mouse. The difference in selection speed between the virtual air mouse and the touchpad was approximately equivalent to the selection speed gap observed between the touchpad and the mouse. These findings indicated that the virtual air mouse constitutes a potentially viable input device.

A regression line was fitted to describe the relationship between mean completion time (MT) and index of difficulty ($ID = \log_2 \frac{2D}{W}$), where the slope served as an index of throughput and the intercept represented the constant time overhead (Fig. 13b). The mouse exhibited the highest throughput ($k = 132.7, TP = 7.5$ bit/s), whereas the touchpad ($k = 387.3, TP = 2.6$ bit/s) and the virtual air mouse ($k = 393.1, TP = 2.5$ bit/s) demonstrated comparable throughput. This indicates that the virtual air mouse and the touchpad exhibit comparable cursor movement speed and similar input performance. The intercept for the virtual air mouse was the highest, reflecting extra constant time overhead caused by hand movement variability in three-dimensional space.

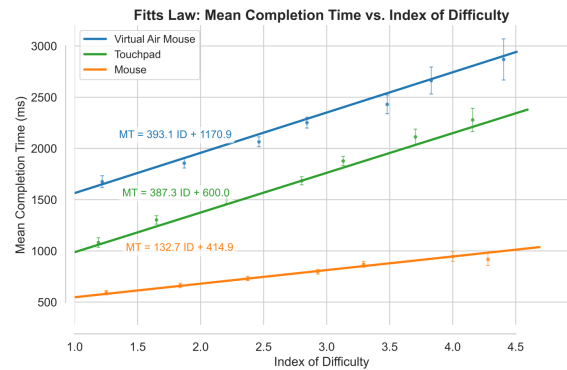
The Fitts' Law study suggested that the virtual air mouse and the touchpad exhibit comparable performance on specific metrics, highlighting the high precision of the hand mesh predictions. These results further suggest that WRISTP² may serve as a portable, lightweight, and precise input modality, capable of supporting interaction in a wide range of contexts.

7.4 USER STUDY 2: Multi-Finger Pressure Control

7.4.1 Design and Procedure. The second study evaluated the system's capability for multi-finger pressure control. During each trial, participants were instructed to press the desk using a specific set of fingers. The system estimated fingertip pressure by aggregating vertex values within predefined fingertip regions on the hand mesh. These pressure estimates were mapped to the GUI, which provided five individual progress bars—one per finger—for fine-grained feedback, along with a combined bar indicating the average pressure of the fingers required in the current trial (Fig. 12). This combined bar served as a reference for coordinating multi-finger input.



(a) Completion time for different input devices.



(b) Fitted line of MT versus ID.

Figure 13: Performance comparison among input devices. (a) Performance was quantified using the median and interquartile range (IQR). (b) For each device, a regression was fitted using the aggregated data across all trials.

At the start of each trial, one of 13 finger combinations was randomly selected, covering single-, two-, three-, four-, and five-finger configurations. These combinations were chosen because they reflect natural and frequently used finger postures during planar hand interactions; their detailed specification is reported in the supplementary. A target pressure range was displayed on the combined bar, with its center uniformly sampled from [500, 1500] g and width from [500, 1500] g. Participants were required to apply force with the specified fingers so that the average pressure remained within the target range for 3 s. A trial was considered a failure if the target range was not reached and stabilized within 10 s. Each participant completed 100 trials.

7.4.2 Measures and Analysis. We recorded the trial outcome (success/failure) and the completion time (CT, s). CT was defined as the time from trial onset until the participant successfully held the pressure within the target range for 3 s. CT was computed only for successful trials. For reporting we summarize success rate (SR, %), as well as the median and interquartile range (IQR) of CT. Figures 14 visualize the median CT and success rate by finger-count. Table 6 summarizes outcomes across finger-count categories.

Table 6: Performance summary aggregated by finger-count with total $N=1800$ distributed by combination sampling ratios (Single/Two/Three/Four/Five = 5/4/2/1/1 out of 13). SR = success rate with 95% CI (Wilson); CT = completion time (successful trials only).

Finger	Trials (N)	Success (N_{succ})	SR (%; 95% CI)	Median CT (s)	IQR CT (s)
Single	692	639	92.4	5.23	2.99
Two	554	444	80.1	7.26	4.42
Three	277	241	87.0	6.69	4.24
Four	138	120	86.7	7.56	5.24
Five	139	116	83.8	7.45	4.07
Overall	1800	1560	86.7	6.10	4.28

Notes: CT statistics are reported on successful trials only.

7.4.3 Results. Overall, participants were consistently able to reach and maintain the target pressure, achieving an average success rate of 86.7% with median completion times around 6 s. This indicates that the system reliably supports stable pressure control under varied interaction settings.

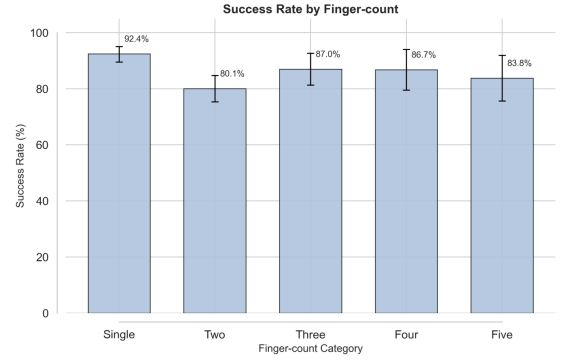
While single-finger input yielded the highest performance (SR=92.4%, median CT= 5.23 s), multi-finger input also reached high success rates in the 80–87% range, albeit with longer completion times (median CT up to 7.56 s) and greater variability. These trends reflect the natural increase in coordination demands as more fingers are involved, yet the overall performance remained robust.

Takeaway. The study demonstrates that the proposed system enables accurate and efficient pressure targeting across different finger combinations. Despite the expected increase in difficulty for multi-finger coordination, participants maintained high success rates and reasonable completion times, underscoring the technique’s suitability for integration into pressure-sensitive interactive applications.

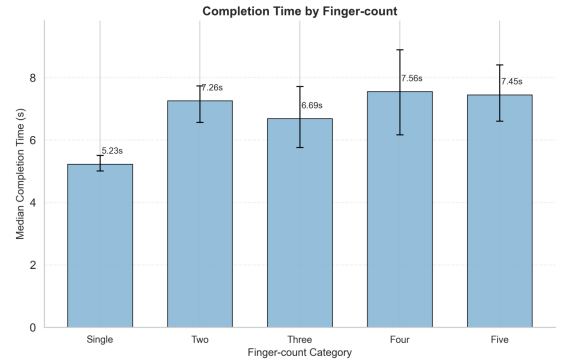
7.5 USER STUDY 3: Virtual Pressure-Sensitive Touchpad

7.5.1 Design and Procedure. The third study evaluated the pressure-sensitive touchpad functionality of WRISTP² in a composite challenging task that couples drag control with pressure. In this study, participants treated the desktop as a virtual pressure-sensitive touchpad. Prior to the trials, participants performed a five-finger contact on the desktop to simultaneously signal session start and define the interaction plane. Using the 3D positions of all five fingertips, we fitted a plane in wrist camera coordinate frame via an SVD-based least-squares procedure: the plane origin was set to the fingertip centroid, and the unit normal \mathbf{n} was taken as the right-singular vector of the centered fingertip coordinates. We then constructed a local orthonormal frame $\{\mathbf{u}, \mathbf{v}, \mathbf{n}\}$ on the plane by projecting the negative camera x -axes onto the plane and normalizing to obtain \mathbf{u} (aligned to the right in the GUI), and setting $\mathbf{v} = \mathbf{n} \times \mathbf{u}$ (pointing downward). Cursor mapping used the fingertip position projected onto this plane and expressed in (\mathbf{u}, \mathbf{v}) coordinates.

In each trial, two on-screen balls were shown: a controllable starting ball with a fixed diameter of 10 mm, and a target ball with



(a) Success rate across finger-count categories.



(b) Median completion time across finger-count categories.

Figure 14: Performance summary across all subjects. (a) Success rate (SR) with 95% CI. (b) Median completion time (MCT) with 95% CI, computed on successful trials only.

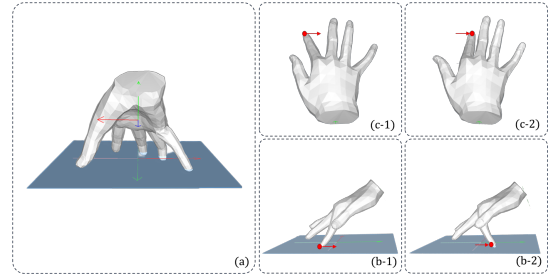


Figure 15: Virtual pressure-sensitive touchpad: (a) definition of the virtual interactive plane; (b–c) scrolling on the plane using the index fingertip.

a radius uniformly sampled from 30 mm to 90 mm. The center-to-center distance between the balls was uniformly sampled from 40 mm to 400 mm, which remained the same as the settings in Section 7.3. To ensure ecological validity while avoiding rarely used gestures, the controlling finger was randomly selected on each trial from *index*, *middle*, and *ring*. These three fingers were chosen because they are the most frequently used for touchpad interaction

Table 7: Performance summary of drag-and-press study with decomposition into total completion time (CT), pressure stabilization time (PST), and movement time (MT). SR = success rate (%); all time statistics are reported on successful trials only.

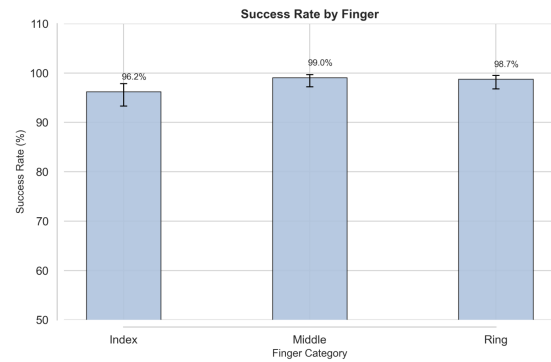
Group	Trials (N)	Success (N _{succ})	SR (%)	Median CT (s)	Median PST (s)	Median MT (s)
Index	339	326	96.2	9.75	5.64	3.36
Middle	367	363	99.0	9.59	5.52	3.45
Ring	374	369	98.7	9.54	5.45	3.88
Overall	1080	1058	98.0	9.59	5.52	3.50

in daily computer use. Participants were asked to drag the starting ball into the target ball's area using the corresponding fingertip (entry when the starting-ball center lay within the target radius). Upon entry, a pressure target range was displayed (same sampling as in Study 2: center uniformly from [500, 1500] g and width from [500, 1500] g). Participants adjusted their pressure so the measured value fell within the range and maintained it for 3 s; the trial was marked *successful* once the 3 s hold completed. Trials that did not reach and stabilize within the range by 15 s were marked *failures*. Each participant completed 60 trials with randomized finger, target size, and distance.

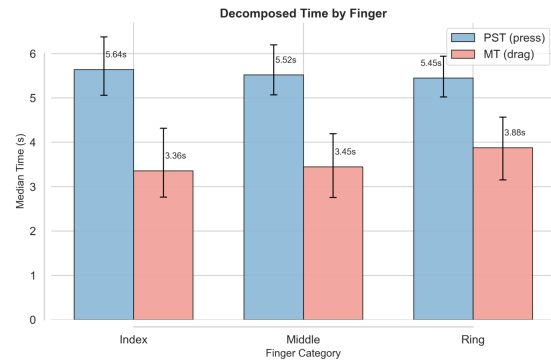
7.5.2 Measures and Analysis. We recorded the trial outcome (success/failure), the movement time (MT, s) and the press stabilization time (PST, s). MT was defined as the time from trial onset until the starting ball entered the target ball. PST was defined as the time from the moment the starting ball entered the target until the pressure was successfully maintained within the target range for 3 s. CT was the sum of MT and PST. Figure 16 visualizes the median MT, PST, CT and success rate by finger categories. Table 7 summarizes outcomes across finger categories.

7.5.3 Results. Overall, participants achieved a high success rate of 98.0% across all trials, with a median total completion time (CT_{total}) of 9.59 s. Notably, this success rate is even higher than in Study 1, despite the drag-and-press task being more challenging; this improvement can be attributed to the longer timeout threshold (15 s vs. 10 s), which allowed participants more time to stabilize their input. The pressure stabilization time (PST) contributed about 5.5 s and the movement time (MT) about 3.5 s. Performance was consistent across index, middle, and ring fingers, with only minor differences.

In terms of success rate, the middle finger (99.0%) and the ring finger (98.7%) performed similarly, while the index finger was slightly lower (96.2%). For pressure stabilization, all three fingers were nearly identical ($PST \approx 5.5$ s), indicating that the pressure control functionality of WRISTP² works reliably and uniformly across fingers. For movement, however, the ring finger required the longest MT (3.88 s), while the index finger was fastest (3.36 s), consistent with their relative flexibility. The middle finger balanced both high success rate and short MT (3.45 s), achieving the best overall performance. This advantage may stem from its position in the fitted interaction plane, where its movements are most naturally aligned with the plane's horizontal and vertical axes.



(a) Success rate across three finger groups.



(b) Decomposed completion time across three finger groups.

Figure 16: Performance summary across all subjects. (a) Success rate (SR) with 95% confidence intervals. (b) Median completion time (CT) decomposed into pressure stabilization time (PST) and movement time (MT), each with 95% confidence intervals, computed on successful trials only.

Takeaway. All three fingers enabled stable drag-and-press performance with WRISTP². While pressure control was equivalent across fingers, drag performance showed finger-specific variation: the index benefited from flexibility, the ring was slower due to reduced dexterity, and the middle finger provided the best balance. These results suggest that, for pressure-sensitive touchpad applications, the middle finger is a reasonable default choice, balancing speed and accuracy.

This study demonstrates the practical value of WRISTP² as a *virtual pressure-sensitive touchpad*, allowing users to perform cursor manipulation and pressure-based input without relying on physical touchpads or mice, thereby enabling more flexible and portable interaction scenarios.

7.6 Subject Feedback

After completing the three lab studies, participants were asked to fill out a subjective questionnaire designed to compare their experiences using WRISTP² with those of traditional mouse and touchpad devices. They were also asked to briefly discuss their overall experience with WRISTP². The questionnaire was based on a 7-point Likert

scale (1 = "Strongly Disagree", 7 = "Strongly Agree") and focused on evaluating the interaction experience across the following five dimensions: 1) comfort (whether prolonged use of the system led to fatigue); 2) ease of use (whether participants were able to quickly master the interaction method); 3) intuitiveness (whether it aligned with human instinctive responses or natural thinking processes); 4) self-efficacy (whether participants felt confident in completing their intended tasks using this interaction method); 5) overall evaluation (participants' holistic assessment of the interaction experience).

The results of the questionnaire are shown in Fig. 17. We conducted statistical analysis of the questionnaire data using the Wilcoxon signed-rank test. The results indicate that WRISTP² outperformed the laptop touchpad on all dimensions, exceeded the mouse in the intuitiveness dimension ($Z = -3.45$, $p < 0.01$), and showed no significant difference compared to the mouse in the other dimensions.

In follow-up interviews, participants frequently highlighted the intuitiveness and naturalness of interacting with WRISTP². Six participants felt that mid-air cursor control with their fingers better matched proprioception than using a touchpad or mouse; seven appreciated the continuous pressure control, especially for tasks such as adjusting sliders; and five believed that integrating WRISTP² into AR/VR could significantly enhance immersion. One participant also noted that resting the wrist while moving a single finger felt easier than using a laptop touchpad. Across tasks, participants' speeds improved by 5.7%, 10.2%, and 14.8% from the first to the second half of the session, suggesting rapid learning.

7.7 Discussion

Across the three lab studies we evaluated WRISTP² as (i) a mid-air cursor device (Study 1), (ii) a multi-finger pressure controller (Study 2), and (iii) a virtual pressure-sensitive touchpad (Study 3). Study 1 showed that while a conventional mouse remained fastest, the virtual air mouse achieved touchpad-level throughput, indicating that WRISTP² can support cursor movement with efficiency close to everyday laptop interaction, albeit with a higher intercept due to 3D hand motion and click confirmation. Study 2 and Study 3 demonstrated that participants could reliably reach and maintain target pressures across single- and multi-finger combinations (overall SR = 86.7% in Study 2 and 98.0% in Study 3).

These findings indicate that WRISTP² affords pose and pressure estimation that is sufficient for both efficient pointing and stable pressure targeting without a physical touch surface. The touchpad-level throughput suggests that WRISTP² can act as a practical alternative when a mouse or touchpad is unavailable (e.g., mobile or standing work, large displays, or XR with table proxies), while the robustness of single- and multi-finger pressure control supports pressure-sensitive shortcuts, sliders, and confirmations on uninstrumented surfaces. Finger-specific trade-offs observed in Study 3 also point to simple defaults, with the middle finger offering a good balance between speed and stability, and the index and ring fingers better suited to fast motion and more relaxed targets, respectively.

Taken together with the large-display application study (Sec. 8.1), these results suggest that WRISTP² is a portable and precise input modality for both pointing and pressure control.

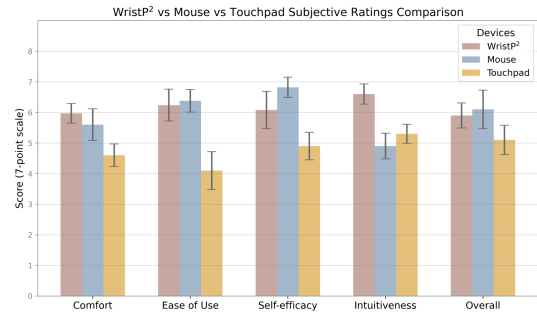


Figure 17: The subjective ratings for different input methods.

8 Application Scenarios

Beyond our controlled studies (Section 7), we illustrate how WRISTP² can be embedded into everyday workflows and evaluate one such scenario in more depth (Study 4). As shown in Fig. 18, WRISTP² supports planar virtual touchpad input and mid-air gestures in XR, air pointing and virtual touchpad control on desktop and mobile devices, and large-display input. These examples show how WRISTP² can span XR, desktop, mobile, and large-display scenarios.

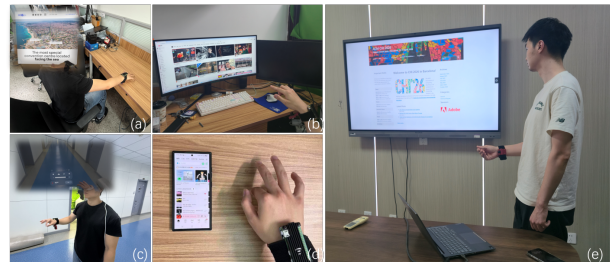


Figure 18: Example application scenarios for WRISTP². (a) Planar virtual touchpad input in extended reality (XR). (b) Air pointing for desktop/PC. (c) Mid-air gesture input in XR. (d) Virtual touchpad input for mobile device control. (e) Controlling slide presentations on a large screen.

8.1 Application Study: Real-World Large-Display Input

To move beyond lab-style tasks and assess one of the large-display scenarios in Fig. 18(e), we conducted a fourth study in a living-room-style setup, comparing WRISTP² against head-mounted, camera-based hand tracking in a Whac-A-Mole game.

8.1.1 Participants. This experiment recruited 12 new participants (2 females, aged 20-26, $M = 23.7$), none of whom had prior experience with the WRISTP² system.

8.1.2 Design and Procedure. As shown in Fig. 19, participants stood approximately 2–2.5 m from a 65-inch display and controlled an on-screen cursor via hand-pose tracking. We compared WRISTP² with



Figure 19: Whac-A-Mole task setup. (a) Participant playing the Whac-A-Mole game using WRISTP². (b) Participant playing the Whac-A-Mole game using a custom head-mounted camera rig.

two representative monocular vision-based hand-tracking methods—MediaPipe [53] and WiLoR [76]—both configured with a head-mounted RGB camera to emulate typical AR/VR usage. Detailed descriptions of the baselines are provided in the Appendix C.1.

All three methods rely on monocular RGB input and were integrated into a unified cursor-mapping pipeline, in which the on-screen cursor was controlled using the index-fingertip position under identical control logic. This design ensures that performance differences can be attributed primarily to hand-tracking quality rather than inconsistencies in input-mapping strategies.

The game board consisted of a 5×5 grid of target locations. On each trial, either a mole or a bomb appeared at a randomly chosen cell. Participants were instructed to hit moles as quickly as possible while avoiding bombs; hitting a mole awarded +1 point, whereas hitting a bomb incurred a −5 point penalty.

Each input method was tested in a single 5-minute game session. The order of methods was counterbalanced across participants, and a 5-minute rest interval was provided between sessions to mitigate fatigue. Game difficulty (e.g., target timing and speed) and session duration were kept constant across conditions to enable a fair comparison between the three input methods.

We aim to answer the following research questions:

RQ1 (Performance): In a real-world large-display task, can WRISTP² achieve better performance (e.g., higher success, shorter time, lower error rate) than head-view approaches?

RQ2 (Effort & Fatigue): Over prolonged use, does WRISTP² reduce perceived workload and fatigue compared to head-view approaches?

8.1.3 Measures and Analysis. In the Whac-A-Mole task, we evaluated task performance using four quantitative metrics: hit rate (**HR**), the proportion of successful mole hits; error rate (**ER**), the proportion of bomb targets mistakenly hit; reaction time (**RT**), the time elapsed between a mole’s appearance and its hit; and the mean game score (**Score**).

After completing all three experimental conditions, participants completed a short subjective questionnaire and were asked to briefly discuss their experiences. Beyond the subjective measures described in Section 7.6, we additionally incorporated a social acceptability measure, evaluating participants’ willingness to use the device in public settings.

8.1.4 Results. For **RQ1 (Performance)**, Table 8 shows that WRISTP² outperformed both head-view baselines on all metrics: it achieved the highest hit rate and game score (HR = 94.47%, Score = 78.92),

Table 8: Task performance comparison (mean ± SD)

Method	HR↑%	ER↓%	RT↓s	Score↑
MediaPipe [53]	86.51 ± 9.79	3.04 ± 2.72	2.19 ± 0.21	61.17 ± 12.66
WiLoR [76]	83.70 ± 8.43	4.57 ± 3.83	2.29 ± 0.20	55.58 ± 12.21
WRISTP² (ours)	94.47 ± 3.64	2.07 ± 0.92	1.43 ± 0.10	78.92 ± 8.30

the lowest error rate (ER = 2.07%), and the shortest reaction time (RT = 1.43 s), with smaller standard deviations. Relative to the two head-mounted methods, this corresponds to an HR gain of about 8–11 percentage points, roughly one-third to one-half lower ER, and 35–40% faster RT, yielding a 30–40% score increase. These gains mainly reflect differences in tracking quality: head-mounted cameras observe the hand from 0.5 m away, where the hand occupies relatively few pixels and is more affected by self-occlusion, whereas WRISTP² maintains a close, wrist-anchored view that produces smoother fingertip trajectories and fewer tracking dropouts. This directly improves rapid target acquisition in the Whac-A-Mole task and answers RQ1 in favor of WRISTP².

For **RQ2 (Effort & Fatigue)**, the configurations differ in ergonomics. Head-mounted tracking requires users to keep the hand within a camera frustum tied to head pose, often inducing larger arm movements to stay in view, while WRISTP² decouples hand input from head orientation and allows small wrist and finger motions in comfortable hand-down postures. Subjective ratings (Fig. 20b) are consistent with this: participants reported lower fatigue and workload and a clear preference for WRISTP² over the head-view conditions. Together, the objective gains and subjective feedback indicate that WRISTP² can reduce perceived effort and fatigue during multi-minute large-display use.

Furthermore, in follow-up interviews, all participants emphasized the smaller movement range and more discreet interaction style afforded by WRISTP², and expressed greater willingness to use it in public settings—consistent with the subjective social acceptability ratings.

9 Limitations and Future Work

Although WRISTP² demonstrates strong performance in 3D hand pose and pressure estimation, it still has certain limitations and areas that warrant further investigation.

Hand-Object Interaction. At present, our work focuses on estimating contact and pressure between the hand and rigid planar or quasi-planar surfaces. However, everyday interaction frequently involves grasping, squeezing, or stabilizing objects of diverse shapes and compliances, where pressure is distributed across curved contact patches and between fingers. Extending WRISTP² to such hand-object scenarios would enable richer applications such as pressure-aware manipulation, adaptive grip control, and safety-critical feedback (e.g., avoiding excessive force on fragile or deformable items). In future work, we plan to expand our dataset by incorporating more object-centric and within-hand interactions, and to estimate pressure both between fingers (e.g., during pinch or clapping) and between the hand and arbitrary objects.

Visual Obstruction. When performing extreme wrist rotations or holding bulky objects, some fingers may be partially or fully

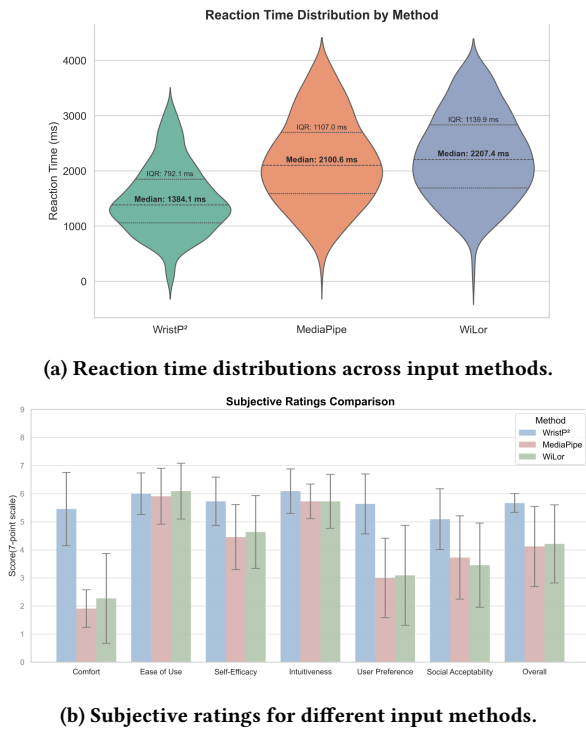


Figure 20: Evaluation results for the Whac-A-Mole study comparing WRISTP² with head-mounted baselines (MediaPipe, WiLoR). (a) WRISTP² achieves significantly lower reaction time (mean 1.43s) and lower variance. (b) Subjective ratings indicate that WRISTP² induces lower fatigue (better Comfort) and is perceived as easier to use compared to head-view approaches. Error bars denote 95% CI.

occluded from the wrist-view camera. A natural next step is to fuse the wrist view with complementary perspectives such as head-mounted or environment-mounted cameras, or with non-visual signals (e.g., EMG, acoustics), so that the system can remain robust when visual coverage is incomplete.

Bimanual Occlusion. Many real-world tasks involve coordinated use of both hands, which often leads to mutual occlusion. While some recent methods [60, 108] can predict bimanual hand poses from external viewpoints in such cases, there is still limited work in HCI that addresses bimanual interaction from ego-centric perspectives. Our current dataset and model focus on a single hand; in future work, we plan to collect bimanual interaction data and extend the model to jointly reason about two hands, enabling pressure-aware collaboration such as two-handed manipulation and cooperative gestures.

Form Factor and On-Device Deployment. Although our prototype achieves wireless deployment and relies on compact off-the-shelf components, the current form factor and power profile still lag behind those of commercial wearable devices that integrate low-power camera modules [48, 100, 103]. The under-wrist camera and electronics can still interfere with certain tabletop postures, and real-world long-term use will require slimmer packaging and tighter

integration into form factors such as smart wristbands or watches. Achieving this will likely require custom hardware (e.g., higher-integration SoCs, flexible PCBs, folded optics) and more stringent power management. In addition, the current model runs at about 22 fps on an NVIDIA RTX4060 GPU, which may limit interaction smoothness and makes direct deployment on low-power wearables challenging. Future work could explore model compression, architecture simplification, and adaptive sampling strategies to support real-time, on-device inference under mobile power and compute budgets.

10 Conclusion

We presented WRISTP², a wrist-worn, camera-based system that reconstructs a full 3D hand mesh and per-vertex pressure from a single RGB frame. Trained on a large wrist-view dataset with high-fidelity pose and pressure annotations, our model achieves low-millimeter pose error and reliable contact and pressure estimation across diverse lighting and surfaces. Four studies show that WRISTP² delivers touchpad-level pointing efficiency, robust multi-finger pressure control, and, in a large-display Whac-A-Mole task, higher task success with lower arm fatigue than head-mounted hand tracking, positioning WRISTP² as a practical wristband platform for pressure-aware interaction on uninstrumented surfaces and in mid-air.

References

- [1] Sang Ho Baek and Kyoung Mu Lee. 2019. Pushing the Envelope for RGB-Based Dense 3D Hand Pose Estimation via Neural Mesh Rendering. In *Proceedings of the IEEE Conference on Computer Vision and Pattern Recognition (CVPR)*. 1067–1076.
- [2] Gereon H. Büscher, Risto Kõiva, Carsten Schürmann, Robert Haschke, and Helge J. Ritter. 2015. Flexible and stretchable fabric-based tactile sensor. *Robotics and Autonomous Systems* 63 (2015), 244–252. doi:10.1016/j.robot.2014.09.007
- [3] Yu-Wei Chao, Wei Yang, Yu Xiang, Pavlo Molchanov, Ankur Handa, Jonathan Tremblay, Yashraj S. Narang, Karl Van Wyk, Umar Iqbal, Stan Birchfield, Jan Kautz, and Dieter Fox. 2021. DexYCB: A Benchmark for Capturing Hand Grasping of Objects. In *Proceedings of the IEEE/CVF Conference on Computer Vision and Pattern Recognition (CVPR)*. 9044–9053.
- [4] Anargyros Chatzitofis, Dimitrios Zarpalas, Stefanos Kollias, and Petros Daras. 2019. DeepMoCap: Deep optical motion capture using multiple depth sensors and retro-reflectors. *Sensors* 19, 2 (2019), 282.
- [5] Feiyu Chen, Honghao Lyu, Zhibo Pang, Junhui Zhang, Yonghong Hou, Ying Gu, Huayong Yang, and Geng Yang. 2019. WristCam: A Wearable Sensor for Hand Trajectory Gesture Recognition and Intelligent Human-Robot Interaction. *IEEE Sensors Journal* 19, 19 (2019), 8441–8451. doi:10.1109/JSEN.2018.2877978
- [6] Nutan Chen, Göran Westling, Benoni B Edin, and Patrick van der Smagt. 2020. Estimating fingertip forces, torques, and local curvatures from fingernail images. *Robotica* 38, 7 (2020), 1242–1262.
- [7] Yi Fei Cheng, Tiffany Luong, Andreas Rene Fender, Paul Strelci, and Christian Holz. 2022. ComforTable User Interfaces: Surfaces Reduce Input Error, Time, and Exertion for Tabletop and Mid-air User Interfaces. In *2022 IEEE International Symposium on Mixed and Augmented Reality (ISMAR)*. 150–159. doi:10.1109/ISMAR55827.2022.00029
- [8] Chiho Choi, Sang Ho Yoon, Chin-Ning Chen, and Karthik Ramani. 2017. Robust hand pose estimation during the interaction with an unknown object. In *Proceedings of the IEEE International Conference on Computer Vision*. 3123–3132.
- [9] Chiho Choi, Sangpil Kim, and Karthik Ramani. 2017. Learning hand articulations by hallucinating heat distribution. In *Proceedings of the IEEE International Conference on Computer Vision*. 3104–3113.
- [10] Peng Dai, Yang Zhang, Tao Liu, Zhen Fan, Tianyuan Du, Zhuo Su, Xiaozheng Zheng, and Zeming Li. 2024. HMD-Poser: On-Device Real-time Human Motion Tracking from Scalable Sparse Observations. In *Proceedings of the IEEE/CVF Conference on Computer Vision and Pattern Recognition (CVPR)*. 874–884.
- [11] Joseph DelPreto, Chao Liu, Yiyue Luo, Michael Foshey, Yunzhu Li, Antonio Torralba, Wojciech Matusik, and Daniela Rus. 2022. ActionSense: a multimodal dataset and recording framework for human activities using wearable sensors in a kitchen environment. , Article 1003 (2022), 14 pages.

- [12] John Dudley, Hrvoje Benko, Daniel Wigdor, and Per Ola Kristensson. 2019. Performance Envelopes of Virtual Keyboard Text Input Strategies in Virtual Reality. In *2019 IEEE International Symposium on Mixed and Augmented Reality (ISMAR)*. 289–300. doi:10.1109/ISMAR.2019.00027
- [13] Camille Dupré, Emmanuel Pietriga, Olivier Gladin, Stéphanie Rey, Houssein Saidi, and Caroline Appert. 2025. Investigating Hand-Bound Pads for AR Input Using Hand-Tracking Only. *Proceedings of the ACM on Human-Computer Interaction* 9, 5 (2025), 1–25.
- [14] Sai Kumar Dwivedi, Yu Sun, Priyanka Patel, Yao Feng, and Michael J Black. 2024. Tokenhmr: Advancing human mesh recovery with a tokenized pose representation. In *Proceedings of the IEEE/CVF conference on computer vision and pattern recognition*. 1323–1333.
- [15] Kiana Ehsani, Shubham Tulsiani, Saurabh Gupta, Ali Farhadi, and Abhinav Gupta. 2020. Use the Force, Luke! Learning to Predict Physical Forces by Simulating Effects. In *Proceedings of the IEEE/CVF Conference on Computer Vision and Pattern Recognition (CVPR)*.
- [16] Guénolé Fiche, Simon Leglaive, Xavier Alameda-Pineda, Antonio Agudo, and Francesc Moreno-Noguer. 2024. Vq-hps: Human pose and shape estimation in a vector-quantized latent space. In *European Conference on Computer Vision*. Springer, 471–490.
- [17] Guénolé Fiche, Simon Leglaive, Xavier Alameda-Pineda, and Francesc Moreno-Noguer. 2025. MEGA: Masked Generative Autoencoder for Human Mesh Recovery. In *Proceedings of the Computer Vision and Pattern Recognition Conference*. 5366–5378.
- [18] Rao Fu, Dingxi Zhang, Alex Jiang, Wanxia Fu, Austin Funk, Daniel Ritchie, and Srinath Sridhar. 2025. GigaHands: A Massive Annotated Dataset of Bimanual Hand Activities. In *Proceedings of the IEEE/CVF Conference on Computer Vision and Pattern Recognition (CVPR)*. 17461–17474.
- [19] Liuhaio Ge, Hui Liang, Junsong Yuan, and Daniel Thalmann. 2016. Robust 3D Hand Pose Estimation in Single Depth Images: From Single-View CNN to Multi-View CNNs. In *Proceedings of the IEEE Conference on Computer Vision and Pattern Recognition (CVPR)*.
- [20] Mucahit Gemici, Vrushank Phadnis, and Anil Ufuk Batmaz. 2025. Before hands disappear: Effect of early warning visual feedback method for hand tracking failures in virtual reality. *PLoS One* 20, 6 (2025), e0323796.
- [21] Patrick Grady, Jeremy A Collins, Chengcheng Tang, Christopher D Twigg, Kunal Aneja, James Hays, and Charles C Kemp. 2024. Pressurevision++: Estimating fingertip pressure from diverse rgb images. In *Proceedings of the IEEE/CVF Winter Conference on Applications of Computer Vision*. 8698–8708.
- [22] Patrick Grady, Chengcheng Tang, Samarth Brahmabhatt, Christopher D Twigg, Chengde Wan, James Hays, and Charles C Kemp. 2022. PressureVision: estimating hand pressure from a single RGB image. In *European Conference on Computer Vision*. Springer, 328–345.
- [23] Shreyas Hampali, Mahdi Rad, Markus Oberweger, and Vincent Lepetit. 2020. Honnotate: A method for 3d annotation of hand and object poses. In *Proceedings of the IEEE/CVF conference on computer vision and pattern recognition*. 3196–3206.
- [24] Shangchen Han, Po-chen Wu, Yubo Zhang, Beibei Liu, Linguang Zhang, Zheng Wang, Weiguang Si, Peizhao Zhang, Yujun Cai, Tomas Hodan, et al. 2022. Ume-Track: Unified multi-view end-to-end hand tracking for VR. In *SIGGRAPH Asia 2022 conference papers*. 1–9.
- [25] Zhe He, Xiangyang Wang, Yuanchun Shi, Chi Hsia, Chen Liang, and Chun Yu. 2025. Palmpad: Enabling Real-Time Index-to-Palm Touch Interaction with a Single RGB Camera. In *Proceedings of the 2025 CHI Conference on Human Factors in Computing Systems*. 1–16.
- [26] Juan David Hincapié-Ramos, Xiang Guo, Paymahn Moghadasian, and Pourang Irani. 2014. Consumed endurance: a metric to quantify arm fatigue of mid-air interactions. In *Proceedings of the SIGCHI Conference on Human Factors in Computing Systems* (Toronto, Ontario, Canada) (CHI '14). Association for Computing Machinery, New York, NY, USA, 1063–1072. doi:10.1145/2556288.2557130
- [27] Fang Hu, Peng He, Songlin Xu, Yin Li, and Cheng Zhang. 2020. FingerTrak: Continuous 3D Hand Pose Tracking by Deep Learning Hand Silhouettes Captured by Miniature Thermal Cameras on Wrist. *Proc. ACM Interact. Mob. Wearable Ubiquitous Technol.* 4, 2, Article 71 (June 2020), 24 pages. doi:10.1145/3397306
- [28] H.H. Hu, A.A. Gooch, W.B. Thompson, B.E. Smits, J.J. Rieser, and P. Shirley. 2000. Visual cues for imminent object contact in realistic virtual environments. In *Proceedings Visualization 2000. VIS 2000 (Cat. No.00CH37145)*. 179–185. doi:10.1109/VISUAL.2000.885692
- [29] Helen H Hu, Amy A Gooch, Sarah H Creem-Regehr, and William B Thompson. 2002. Visual cues for perceiving distances from objects to surfaces. *Presence: Teleoperators & Virtual Environments* 11, 6 (2002), 652–664. doi:10.1162/105474602321050758
- [30] Xinxin Huang, Yunan Xue, Shuyun Ren, and Fei Wang. 2023. Sensor-based wearable systems for monitoring human motion and posture: a review. *Sensors* 23, 22 (2023), 9047.
- [31] Inwook Hwang, Hyungki Son, and Jin Ryong Kim. 2017. AirPiano: Enhancing music playing experience in virtual reality with mid-air haptic feedback. In *2017 IEEE World Haptics Conference (WHC)*. 213–218. doi:10.1109/WHC.2017.7989903
- [32] Wonjun Hwang and Soo-Chul Lim. 2017. Inferring interaction force from visual information without using physical force sensors. *Sensors* 17, 11 (2017), 2455.
- [33] IMOO. 2025. IMOO: Official Website. <https://www.imoo.com/en>
- [34] Yasha Irvantchi, Yang Zhang, Evi Bernitsas, Mayank Goel, and Chris Harrison. 2019. Interferi: Gesture Sensing using On-Body Acoustic Interferometry. In *Proceedings of the 2019 CHI Conference on Human Factors in Computing Systems* (Glasgow, Scotland Uk) (CHI '19). Association for Computing Machinery, New York, NY, USA, 1–13. doi:10.1145/3290605.3300506
- [35] Sujin Jang, Wolfgang Stuerzlinger, Satyajit Ambike, and Karthik Ramani. 2017. Modeling Cumulative Arm Fatigue in Mid-Air Interaction based on Perceived Exertion and Kinetics of Arm Motion. In *Proceedings of the 2017 CHI Conference on Human Factors in Computing Systems* (Denver, Colorado, USA) (CHI '17). Association for Computing Machinery, New York, NY, USA, 3328–3339. doi:10.1145/3025453.3025523
- [36] Hanseok Jeong, Junghoon Seo, and Sang Ho Yoon. 2025. Thumb Force Estimation with Egocentric Vision. In *Adjunct Proceedings of the 38th Annual ACM Symposium on User Interface Software and Technology*. 1–3.
- [37] Shuo Jiang, Bo Lv, Weichao Guo, Chao Zhang, Haitao Wang, Xinjun Sheng, and Peter B. Shull. 2018. Feasibility of Wrist-Worn, Real-Time Hand, and Surface Gesture Recognition via sEMG and IMU Sensing. *IEEE Transactions on Industrial Informatics* 14, 8 (2018), 3376–3385. doi:10.1109/TII.2017.2779814
- [38] Tao Jiang, Peng Lu, Li Zhang, Ningsheng Ma, Rui Han, Chengqi Lyu, Yining Li, and Kai Chen. 2023. RTMPose: Real-Time Multi-Person Pose Estimation based on MMPose. doi:10.48550/ARXIV.2303.07399
- [39] Patrick Kaifosh and Thomas R Reardon. 2025. A generic non-invasive neuromotor interface for human-computer interaction. *Nature* (2025), 1–10. doi:10.1038/s41586-025-09255-w
- [40] Korrawe Karunratanakul, Sergey Prokudin, Otmar Hilliges, and Siyu Tang. 2023. Harp: Personalized hand reconstruction from a monocular rgb video. In *Proceedings of the IEEE/CVF conference on computer vision and pattern recognition*. 12802–12813.
- [41] Renta KASAI, Kazuhiko SASAGAWA, Kazuhiro FUJISAKI, Satoshi SAITO, and Hiroshi KOYAMA. 2018. Development of contact pressure and shear stresses sensor for touch panel. *Mechanical Engineering Letters* 4 (2018), 18–00257.
- [42] Leyla Khaleghi, Alireza Sepas-Moghaddam, Joshua Marshall, and Ali Etamad. 2022. Multiview video-based 3-d hand pose estimation. *IEEE Transactions on Artificial Intelligence* 4, 4 (2022), 896–909.
- [43] David Kim, Otmar Hilliges, Shahram Izadi, Alex D. Butler, Jiawen Chen, Iason Ikononmidis, and Patrick Olivier. 2012. Digits: freehand 3D interactions anywhere using a wrist-worn gloveless sensor. In *Proceedings of the 25th Annual ACM Symposium on User Interface Software and Technology* (Cambridge, Massachusetts, USA) (UIST '12). Association for Computing Machinery, New York, NY, USA, 167–176. doi:10.1145/2380116.2380139
- [44] Minwo Kim, Jaechan Cho, Seongjoo Lee, and Yunho Jung. 2019. IMU Sensor-Based Hand Gesture Recognition for Human-Machine Interfaces. *Sensors* 19, 18 (2019). doi:10.3390/s19183827
- [45] Kenrick Kin, Chengde Wan, Ken Koh, Andrei Marin, Necati Cihan Camgöz, Yubo Zhang, Yujun Cai, Fedor Kovalev, Moshe Ben-Zacharia, Shannon Hoople, Marcos Nunes-Ueno, Mariel Sanchez-Rodriguez, Ayush Bhargava, Robert Wang, Eric Sausser, and Shugao Ma. 2024. STMG: A Machine Learning Microgesture Recognition System for Supporting Thumb-Based VR/AR Input. In *Proceedings of the 2024 CHI Conference on Human Factors in Computing Systems* (Honolulu, HI, USA) (CHI '24). Association for Computing Machinery, New York, NY, USA, Article 753, 15 pages. doi:10.1145/3613904.3642702
- [46] Dominik Kulon, Hsiao-Yu Fish Tung, Tomas Simon, Takaaki Shiratori, and Roberto Cipolla. 2020. Weakly-Supervised 3D Hand Pose Estimation from Monocular RGB Images. In *Proceedings of the European Conference on Computer Vision (ECCV)*.
- [47] Alexander Kyu, Hongyu Mao, Junyi Zhu, Mayank Goel, and Karan Ahuja. 2024. Eitpose: Wearable and practical electrical impedance tomography for continuous hand pose estimation. In *Proceedings of the 2024 CHI Conference on Human Factors in Computing Systems*. 1–10.
- [48] Brilliant Labs. 2025. Brilliant Labs Frame. <https://brilliant.xyz/products/frame>
- [49] Chi-Jung Lee, Ruidong Zhang, Devansh Agarwal, Tianhong Catherine Yu, Vipin Gunda, Oliver Lopez, James Kim, Sicheng Yin, Boao Dong, Ke Li, Mose Sakashita, Francois Guimbretiere, and Cheng Zhang. 2024. EchoWrist: Continuous Hand Pose Tracking and Hand-Object Interaction Recognition Using Low-Power Active Acoustic Sensing On a Wristband. In *Proceedings of the 2024 CHI Conference on Human Factors in Computing Systems* (Honolulu, HI, USA) (CHI '24). Association for Computing Machinery, New York, NY, USA, Article 403, 21 pages. doi:10.1145/3613904.3642910
- [50] Jiye Lee and Hanbyul Joo. 2024. Mocap Everyone Everywhere: Lightweight Motion Capture With Smartwatches and a Head-Mounted Camera. In *Proceedings of the IEEE/CVF Conference on Computer Vision and Pattern Recognition (CVPR)*. 1091–1100.
- [51] Chentao Li, Ziheng Xi, Jianjiang Feng, and Jie Zhou. 2025. FineType: Fine-grained Tapping Gesture Recognition for Text Entry. In *Proceedings of the 2025 CHI Conference on Human Factors in Computing Systems* (CHI '25). Association

- for Computing Machinery, New York, NY, USA, Article 1083, 20 pages. doi:10.1145/3706598.3714278
- [52] Zongmian Li, Jiri Sedlar, Justin Carpentier, Ivan Laptev, Nicolas Mansard, and Josef Sivic. 2019. Estimating 3D Motion and Forces of Person-Object Interactions From Monocular Video. In *Proceedings of the IEEE/CVF Conference on Computer Vision and Pattern Recognition (CVPR)*.
- [53] Camillo Lugaresi, Jiuqiang Tang, Hadon Nash, Chris McClanahan, Esha Ubowaja, Michael Hays, Fan Zhang, Chuo-Ling Chang, Ming Guang Yong, Juhyun Lee, et al. 2019. Mediapipe: A framework for building perception pipelines. *arXiv preprint arXiv:1906.08172* (2019).
- [54] Naureen Mahmood, Nima Ghorbani, Nikolaus F Troje, Gerard Pons-Moll, and Michael J Black. 2019. AMASS: Archive of motion capture as surface shapes. In *Proceedings of the IEEE/CVF international conference on computer vision*. 5442–5451.
- [55] Jameel Malik, Ahmed Elhayek, and Didier Stricker. 2017. 3D Hand Shape and Pose Estimation from a Single RGB Image. In *Proceedings of the IEEE International Conference on Image Processing (ICIP)*.
- [56] Yumin Mao, Uksang Yoo, Yunchao Yao, Shahram Najam Syed, Luca Bondi, Jonathan Francis, Jean Oh, and Jeffrey Ichnowski. 2025. Visuo-Acoustic Hand Pose and Contact Estimation. *arXiv preprint arXiv:2508.00852* (2025).
- [57] S.A. Mascaro and H.H. Asada. 2001. Photoplethysmograph fingernail sensors for measuring finger forces without haptic obstruction. *IEEE Transactions on Robotics and Automation* 17, 5 (2001), 698–708. doi:10.1109/70.964669
- [58] S.A. Mascaro and H.H. Asada. 2004. Measurement of finger posture and three-axis fingertip touch force using fingernail sensors. *IEEE Transactions on Robotics and Automation* 20, 1 (2004), 26–35. doi:10.1109/TRA.2003.820931
- [59] Jess McIntosh, Asier Marzo, and Mike Fraser. 2017. SensIR: Detecting Hand Gestures with a Wearable Bracelet using Infrared Transmission and Reflection. In *Proceedings of the 30th Annual ACM Symposium on User Interface Software and Technology (Québec City, QC, Canada) (UIST '17)*. Association for Computing Machinery, New York, NY, USA, 593–597. doi:10.1145/3126594.3126604
- [60] Hao Meng, Sheng Jin, Wentao Liu, Chen Qian, Mengxiang Lin, Wanli Ouyang, and Ping Luo. 2022. 3d interacting hand pose estimation by hand de-occlusion and removal. In *European Conference on Computer Vision*. Springer, 380–397.
- [61] Inc. Meta Platforms. 2022. Meta Quest 2. <https://www.meta.com/quest/>
- [62] Meta Platforms, Inc. 2024. Orion: True Augmented Reality Glasses. <https://about.meta.com/realitylabs/orion/>
- [63] Meta Reality Labs. 2020. Project Aria: A Research Tool for Augmented Reality. <https://www.projectaria.com/>
- [64] Vimal Mollyn and Chris Harrison. 2024. EgoTouch: On-Body Touch Input Using AR/VR Headset Cameras. In *Proceedings of the 37th Annual ACM Symposium on User Interface Software and Technology (Pittsburgh, PA, USA) (UIST '24)*. Association for Computing Machinery, New York, NY, USA, Article 69, 11 pages. doi:10.1145/3654777.3676455
- [65] Gyeongsik Moon, Ju Yong Chang, and Kyoung Mu Lee. 2018. V2v-posenet: Voxel-to-voxel prediction network for accurate 3d hand and human pose estimation from a single depth map. In *Proceedings of the IEEE conference on computer vision and pattern recognition*. 5079–5088.
- [66] Gyeongsik Moon, Ju Yong Chang, and Kyoung Mu Lee. 2018. V2V-PoseNet: Voxel-to-Voxel Prediction Network for Accurate 3D Hand and Human Pose Estimation from a Single Depth Map. In *Proceedings of the IEEE Conference on Computer Vision and Pattern Recognition (CVPR)*. 5079–5088.
- [67] Gyeongsik Moon, Shou-I Yu, He Wen, Takaaki Shiratori, and Kyoung Mu Lee. 2020. Interhand2. 6m: A dataset and baseline for 3d interacting hand pose estimation from a single rgb image. In *European Conference on Computer Vision*. Springer, 548–564.
- [68] Franziska Mueller, Micah Davis, Florian Bernard, Oleksandr Sotnychenko, Mickael Verschoor, Miguel A Otaduy, Dan Casas, and Christian Theobalt. 2019. Real-time pose and shape reconstruction of two interacting hands with a single depth camera. *ACM Transactions on Graphics (ToG)* 38, 4 (2019), 1–13.
- [69] Franziska Mueller, Dushyant Mehta, Oleksandr Sotnychenko, Srinath Sridhar, Dan Casas, and Christian Theobalt. 2017. Real-Time Hand Tracking Under Occlusion From an Egocentric RGB-D Sensor. In *Proceedings of the IEEE International Conference on Computer Vision (ICCV)*.
- [70] Chaithanya Kumar Mummadi, Frederic Philips Peter Leo, Keshav Deep Verma, Shivaji Kasireddy, Philipp M. Scholl, Jochen Kempfle, and Kristof Van Laerhoven. 2018. Real-Time and Embedded Detection of Hand Gestures with an IMU-Based Glove. *Informatics* 5, 2 (2018). doi:10.3390/informatics5020028
- [71] Iason Oikonomidis, Nikolaos Kyriazis, and Antonis Argyros. 2011. Efficient model-based 3d tracking of hand articulations using kinect. In *Proceedings of the British Machine Vision Conference 2011*.
- [72] Omate. 2013. Omate TrueSmart: Standalone Smartwatch 2.0. <http://www.omate.com>
- [73] Georgios Pavlakos, Dandan Shan, Ilija Radosavovic, Angjoo Kanazawa, David Fouhey, and Jitendra Malik. 2024. Reconstructing Hands in 3D with Transformers. In *Proceedings of the IEEE/CVF Conference on Computer Vision and Pattern Recognition (CVPR)*. 9826–9836.
- [74] Tu-Hoa Pham, Nikolaos Kyriazis, Antonis A. Argyros, and Abderrahmane Kheddar. 2018. Hand-Object Contact Force Estimation from Markerless Visual Tracking. *IEEE Transactions on Pattern Analysis and Machine Intelligence* 40, 12 (2018), 2883–2896. doi:10.1109/TPAMI.2017.2759736
- [75] Rolandos Alexandros Potamias, Stylianos Ploumpis, Stylianos Moschoglou, Vasileios Triantafyllou, and Stefanos Zafeiriou. 2023. Handy: Towards a High Fidelity 3D Hand Shape and Appearance Model. In *Proceedings of the IEEE/CVF Conference on Computer Vision and Pattern Recognition (CVPR)*. 4670–4680.
- [76] Rolandos Alexandros Potamias, Jinglei Zhang, Jiankang Deng, and Stefanos Zafeiriou. 2025. WiLoR: End-to-end 3D Hand Localization and Reconstruction in-the-wild. In *Proceedings of the IEEE/CVF Conference on Computer Vision and Pattern Recognition (CVPR)*. 12242–12254.
- [77] Pressure Profile. 2025. Pressure Profile: Official Website. <https://pressureprofile.com/home>
- [78] Dennis Reimer, Iana Podkosova, Daniel Scherzer, and Hannes Kaufmann. 2023. Evaluation and improvement of HMD-based and RGB-based hand tracking solutions in VR. *Frontiers in Virtual Reality* 4 (2023), 1169313.
- [79] Rokid. 2024. Rokid AR Lite: Spatial Computing Suite. <https://global.rokid.com/>
- [80] Javier Romero, Dimitrios Tzionas, and Michael J. Black. 2017. Embodied hands: modeling and capturing hands and bodies together. *ACM Transactions on Graphics* 36, 6 (Nov. 2017), 1–17. doi:10.1145/3130800.3130883
- [81] Farshid Salemi Parizi, Wolf Kienzle, Eric Whitmire, Aakar Gupta, and Hrvoje Benko. 2021. RotoWrist: Continuous Infrared Wrist Angle Tracking using a Wristband. In *Proceedings of the 27th ACM Symposium on Virtual Reality Software and Technology (Osaka, Japan) (VRST '21)*. Association for Computing Machinery, New York, NY, USA, Article 26, 11 pages. doi:10.1145/3489849.3489886
- [82] Sasha Salter, Richard Warren, Collin Schlager, Adrian Spurr, Shangchen Han, Rohin Bhasin, Yujun Cai, Peter Walkington, Anuoluwapo Bolarinwa, Robert Wang, Nathan Danielson, Josh Merel, Eftychiou Pnevmatikakis, and Jesse Marshall. 2024. emg2pose: A Large and Diverse Benchmark for Surface Electromyographic Hand Pose Estimation. In *Advances in Neural Information Processing Systems*, A. Globerson, L. Mackey, D. Belgrave, A. Fan, U. Paquet, J. Tomczak, and C. Zhang (Eds.), Vol. 37. Curran Associates, Inc., 55703–55728. https://proceedings.neurips.cc/paper_files/paper/2024/file/64f8884f6ba3d9ace5bb647c4f917896-Paper-Datasets_and_Benchmarks_Track.pdf
- [83] Gaspare Santaera, Emanuele Luberto, Alessandro Serio, Marco Gabiccini, and Antonio Bicchi. 2015. Low-cost, fast and accurate reconstruction of robotic and human postures via IMU measurements. In *2015 IEEE International Conference on Robotics and Automation (ICRA)*. 2728–2735. doi:10.1109/ICRA.2015.7139569
- [84] Davide Scaramuzza, Agostino Martinelli, and Roland Siegwart. 2006. A toolbox for easily calibrating omnidirectional cameras. In *2006 IEEE/RSJ International Conference on Intelligent Robots and Systems*. IEEE, 5695–5701.
- [85] Arindam Sengupta, Feng Jin, Renyuan Zhang, and Siyuan Cao. 2020. mm-Pose: Real-Time Human Skeletal Posture Estimation Using mmWave Radars and CNNs. *IEEE Sensors Journal* 20, 17 (2020), 10032–10044. doi:10.1109/JSEN.2020.2991741
- [86] Sensel. 2025. *Sensel Morph: A Force-Sensing Input Device*. <https://sensel.com>
- [87] Kyungjin Seo, Junghoon Seo, Hanseok Jeong, Sangpil Kim, and Sang Ho Yoon. 2024. Posture-informed muscular force learning for robust hand pressure estimation. *Advances in Neural Information Processing Systems* 37 (2024), 87831–87873.
- [88] Xiyuan Shen, Chun Yu, Xutong Wang, Chen Liang, Haozhan Chen, and Yuanchun Shi. 2024. MouseRing: Always-available Touchpad Interaction with IMU Rings. In *Proceedings of the CHI Conference on Human Factors in Computing Systems*. ACM, Honolulu HI USA, 1–19. doi:10.1145/3613904.3642225
- [89] Prajwal Shenoy, Anurag Gupta, and Varadhan S.K.M. 2022. Design and Validation of an IMU Based Full Hand Kinematic Measurement System. *IEEE Access* 10 (2022), 93812–93830. doi:10.1109/ACCESS.2022.3203186
- [90] Yilei Shi, Haimo Zhang, Jiashuo Cao, and Suranga Nanayakkara. 2020. VersaTouch: A Versatile Plug-and-Play System that Enables Touch Interactions on Everyday Passive Surfaces. In *Proceedings of the Augmented Humans International Conference (Kaiserslautern, Germany) (AHs '20)*. Association for Computing Machinery, New York, NY, USA, Article 26, 12 pages. doi:10.1145/3384657.3384778
- [91] Paul Strel, Rayan Armani, Yi Fei Cheng, and Christian Holz. 2023. HOOV: Hand Out-Of-View Tracking for Proprioceptive Interaction using Inertial Sensing. In *Proceedings of the 2023 CHI Conference on Human Factors in Computing Systems (Hamburg, Germany) (CHI '23)*. Association for Computing Machinery, New York, NY, USA, Article 310, 16 pages. doi:10.1145/3544548.3581468
- [92] Paul Strel, Jiayi Jiang, Andreas Rene Fender, Manuel Meier, Hugo Romat, and Christian Holz. 2022. TapType: Ten-finger text entry on everyday surfaces via Bayesian inference. In *Proceedings of the 2022 CHI Conference on Human Factors in Computing Systems (New Orleans, LA, USA) (CHI '22)*. Association for Computing Machinery, New York, NY, USA, Article 497, 16 pages. doi:10.1145/3491102.3501878
- [93] Paul Strel, Mark Richardson, Fadi Botros, Shugao Ma, Robert Wang, and Christian Holz. 2024. TouchInsight: Uncertainty-aware Rapid Touch and Text Input for Mixed Reality from Egocentric Vision. In *Proceedings of the 37th Annual ACM Symposium on User Interface Software and Technology*. 1–16.

- [94] Subramanian Sundaram, Petr Kellnhofer, Yunzhu Li, Jun-Yan Zhu, Antonio Torralba, and Wojciech Matusik. 2019. Learning the signatures of the human grasp using a scalable tactile glove. *Nature* 569, 7758 (2019), 698–702.
- [95] James S Supancic, Grégory Rogez, Yi Yang, Jamie Shotton, and Deva Ramanan. 2015. Depth-based hand pose estimation: data, methods, and challenges. In *Proceedings of the IEEE international conference on computer vision*. 1868–1876.
- [96] Andrea Tagliasacchi, Matthias Schröder, Anastasia Tkach, Sofien Bouaziz, Mario Botsch, and Mark Pauly. 2015. Robust articulated-icp for real-time hand tracking. In *Computer graphics forum*, Vol. 34. Wiley Online Library, 101–114.
- [97] Danhang Tang, Hyung Jin Chang, Alykhan Tejani, and Tae-Kyun Kim. 2014. Latent Regression Forest: Structured Estimation of 3D Articulated Hand Posture. In *Proceedings of the IEEE Conference on Computer Vision and Pattern Recognition (CVPR)*. 3786–3793.
- [98] Tekscan. 2025. Pressure Mapping Sensors. <https://www.tekscan.com/>
- [99] Jonathan Tompson, Murphy Stein, Yann Lecun, and Ken Perlin. 2014. Real-Time Continuous Pose Recovery of Human Hands Using Convolutional Networks. In *Proceedings of the IEEE Conference on Computer Vision and Pattern Recognition (CVPR)*. 2141–2148.
- [100] Marc Tonsen, Chris Kay Baumann, and Kai Dierkes. 2020. A high-level description and performance evaluation of pupil invisible. *arXiv preprint arXiv:2009.00508* (2020).
- [101] Hoang Truong, Shuo Zhang, Ufuk Muncuk, Phuc Nguyen, Nam Bui, Anh Nguyen, Qin Lv, Kaushik Chowdhury, Thang Dinh, and Tam Vu. 2018. CapBand: Battery-free Successive Capacitance Sensing Wristband for Hand Gesture Recognition. In *Proceedings of the 16th ACM Conference on Embedded Networked Sensor Systems* (Shenzhen, China) (*SensSys '18*). Association for Computing Machinery, New York, NY, USA, 54–67. doi:10.1145/3274783.3274854
- [102] Hanyue Tu, Chunyu Wang, and Wenjun Zeng. 2020. Voxelpose: Towards multi-camera 3d human pose estimation in wild environment. In *European conference on computer vision*. Springer, 197–212.
- [103] Tap With Us. 2023. TapXR: A Wearable Input Device. <https://www.tapwithus.com/product/tap-xr/>
- [104] Maria Valero, Nick Hale, Jing Tang, Liudi Jiang, Mike McGrath, Jianliang Gao, Piotr Laszczak, and David Moser. 2016. Interfacial pressure and shear sensor system for fingertip contact applications. *Healthcare Technology Letters* 3, 4 (2016), 280–283.
- [105] Aaron van den Oord, Oriol Vinyals, and koray kavukcuoglu. 2017. Neural Discrete Representation Learning. In *Advances in Neural Information Processing Systems*, I. Guyon, U. Von Luxburg, S. Bengio, H. Wallach, R. Fergus, S. Vishwanathan, and R. Garnett (Eds.), Vol. 30. Curran Associates, Inc. https://proceedings.neurips.cc/paper_files/paper/2017/file/7a98af17e63a0ac09ce2e96d03992fbc-Paper.pdf
- [106] Ashish Vaswani, Noam Shazeer, Niki Parmar, Jakob Uszkoreit, Llion Jones, Aidan N Gomez, Lukasz Kaiser, and Illia Polosukhin. 2017. Attention is all you need. *Advances in neural information processing systems* 30 (2017).
- [107] Uta Wagner, Andreas Asferg Jacobsen, Tiare Feuchtner, Hans Gellersen, and Ken Pfeuffer. 2024. Eye-Hand Movement of Objects in Near Space Extended Reality. In *Proceedings of the 37th Annual ACM Symposium on User Interface Software and Technology* (Pittsburgh, PA, USA) (*UIST '24*). Association for Computing Machinery, New York, NY, USA, Article 84, 13 pages. doi:10.1145/3654777.3676446
- [108] Congyi Wang, Feida Zhu, and Shilei Wen. 2023. MeMaHand: Exploiting Mesh-Mano Interaction for Single Image Two-Hand Reconstruction. In *Proceedings of the IEEE/CVF Conference on Computer Vision and Pattern Recognition (CVPR)*. 564–573.
- [109] Erwin Wu, Ye Yuan, Hui-Shyong Yeo, Aaron Quigley, Hideki Koike, and Kris M. Kitani. 2020. Back-Hand-Pose: 3D Hand Pose Estimation for a Wrist-worn Camera via Dorsum Deformation Network. In *Proceedings of the 33rd Annual ACM Symposium on User Interface Software and Technology* (Virtual Event, USA) (*UIST '20*). Association for Computing Machinery, New York, NY, USA, 1147–1160. doi:10.1145/3379337.3415897
- [110] Jianxiong Xiao, Krista A Ehinger, Aude Oliva, and Antonio Torralba. 2012. Recognizing scene viewpoint using panoramic place representation. In *2012 IEEE conference on computer vision and pattern recognition*. IEEE, 2695–2702.
- [111] Chi Xu and Li Cheng. 2013. Efficient hand pose estimation from a single depth image. In *Proceedings of the IEEE international conference on computer vision*. 3456–3462.
- [112] Lixin Yang, Xinyu Zhan, Kailin Li, Wenqiang Xu, Jiefeng Li, and Cewu Lu. 2021. CPF: Learning a Contact Potential Field to Model the Hand-Object Interaction. In *ICCV*.
- [113] Tianhong Catherine Yu, Guilin Hu, Ruidong Zhang, Hyunchul Lim, Saif Mahmud, Chi-Jung Lee, Ke Li, Devansh Agarwal, Shuyang Nie, Jinseok Oh, et al. 2024. Ring-a-Pose: A Ring for Continuous Hand Pose Tracking. *Proceedings of the ACM on Interactive, Mobile, Wearable and Ubiquitous Technologies* 8, 4 (2024), 1–30.
- [114] Shanxin Yuan, Qi Ye, Bjorn Stenger, Siddhant Jain, and Tae-Kyun Kim. 2017. BigHand2.2M Benchmark: Hand Pose Dataset and State of the Art Analysis. In *Proceedings of the IEEE Conference on Computer Vision and Pattern Recognition (CVPR)*.
- [115] Yang Zhang and Chris Harrison. 2015. Tomo: Wearable, Low-Cost Electrical Impedance Tomography for Hand Gesture Recognition. In *Proceedings of the 28th Annual ACM Symposium on User Interface Software & Technology* (Charlotte, NC, USA) (*UIST '15*). Association for Computing Machinery, New York, NY, USA, 167–173. doi:10.1145/2807442.2807480
- [116] Yang Zhang, Robert Xiao, and Chris Harrison. 2016. Advancing Hand Gesture Recognition with High Resolution Electrical Impedance Tomography. In *Proceedings of the 29th Annual Symposium on User Interface Software and Technology* (Tokyo, Japan) (*UIST '16*). Association for Computing Machinery, New York, NY, USA, 843–850. doi:10.1145/2984511.2984574
- [117] Yiming Zhao, Taein Kwon, Paul Strelci, Marc Pollefeys, and Christian Holz. 2025. EgoPressure: A dataset for hand pressure and pose estimation in egocentric vision. In *Proceedings of the Computer Vision and Pattern Recognition Conference*. 27727–27738.
- [118] Yi Zhou, Connelly Barnes, Jingwan Lu, Jimei Yang, and Hao Li. 2019. On the continuity of rotation representations in neural networks. In *Proceedings of the IEEE/CVF conference on computer vision and pattern recognition*. 5745–5753.
- [119] Yi Zhou, Chenglei Wu, Zimo Li, Chen Cao, Yuting Ye, Jason Saragih, Hao Li, and Yaser Sheikh. 2020. Fully convolutional mesh autoencoder using efficient spatially varying kernels. *Advances in neural information processing systems* 33 (2020), 9251–9262.
- [120] Christian Zimmermann, Max Argus, and Thomas Brox. 2021. Contrastive representation learning for hand shape estimation. In *DAGM German Conference on Pattern Recognition*. Springer, 250–264.
- [121] Christian Zimmermann and Thomas Brox. 2017. Learning to Estimate 3D Hand Pose from Single RGB Images. In *Proceedings of the IEEE International Conference on Computer Vision (ICCV)*. 4913–4921.
- [122] Christian Zimmermann, Duygu Ceylan, Jimei Yang, Bryan Russell, Max Argus, and Thomas Brox. 2019. FreiHAND: A Dataset for Markerless Capture of Hand Pose and Shape From Single RGB Images. In *Proceedings of the IEEE/CVF International Conference on Computer Vision (ICCV)*.

A Extended Details About Dataset

In this section, we provide a complete list and detailed definitions of gestures in the WRISTP² dataset in Section 4.

A.1 On-plane Gestures

The on-plane gestures we designed include 48 actions, consisting of common actions using pressure-sensitive touchpads, as well as additional complex actions to increase the diversity of touch data. The descriptions of these gestures are shown in Table 9 below:

A.2 Mid-air Gestures

Mid-air gestures encompass static standard sign language, including 10 American Sign Language (ASL) alphabet letters and 18 common daily interaction gestures. The names and illustrations of these gestures are shown in Fig. 21 below:

B Detailed Algorithmic Design

B.1 Canonical Hand-Local Coordinate Frame

As described in Section 4.4.1, to provide a consistent reference frame across participants and sessions, we introduce a hand-local canonical coordinate system, which serves as the basis for both annotation optimization and network prediction. Unlike externally measured frames (e.g., world or camera coordinates), this local frame is defined algorithmically from anatomical landmarks on the hand mesh. Specifically, the origin is placed at the wrist joint, the x -axis is aligned with the vector from the wrist to the index MCP joint, and the palm normal—computed as the cross product between the wrist-index vector and the wrist-pinky vector—defines the z -axis. The y -axis is then derived to complete a right-handed orthogonal system. We additionally enforce $\det(R) = 1$ and flip the palm normal

Table 9: On-plane Series Gestures

No.	Action Description	No.	Action Description
1	Thumb pulp press	2	Thumb tip press
3	Middle pulp press	4	Middle tip press
5	Index pulp press	6	Index tip press
7	Ring pulp press	8	Ring tip press
9	Pinky pulp press	10	Pinky tip press
11	Two-finger pulp press	12	Two-finger tip press
13	Three-finger pulp press	14	Three-finger tip press
15	Four-finger pulp press	16	Four-finger tip press
17	Five-finger pulp press	18	Five-finger tip press
19	Thumb press, move horizontally and vertically	20	Index press, move horizontally and vertically
21	Middle press, move horizontally and vertically	22	Ring press, move horizontally and vertically
23	Pinky press, move horizontally and vertically	24	Two-finger press, move horizontally and vertically
25	Three-finger press, move horizontally and vertically	26	Four-finger press, move horizontally and vertically
27	Five-finger press, move horizontally and vertically	28	Thumb press, circular motion
29	Index press, circular motion	30	Middle press, circular motion
31	Ring press, circular motion	32	Pinky press, circular motion
33	Two-finger light touch, pinch	34	Two-finger press, pinch
35	Five-finger light touch, clench	36	Five-finger press, clench
37	Thumb rotation, continuous press	38	Index rotation, continuous press
39	Middle rotation, continuous press	40	Ring rotation, continuous press
41	Pinky rotation, continuous press	42	Thumb roll press
43	Middle roll press	44	Index roll press
45	Ring roll press	46	Pinky roll press
47	Palm side press	48	Palm center press

if necessary to ensure consistent orientation across subjects and sessions.

We denote this canonical hand-local frame as $\{H\}$, the world frame as $\{W\}$, and the camera frame as $\{C\}$. A point \mathbf{x}_W expressed in the world frame is mapped into $\{H\}$ by

$$\mathbf{x}_H = \mathbf{T}_W^H \mathbf{x}_W, \quad \mathbf{T}_W^H = \begin{bmatrix} R_{H \leftarrow W} & t_{H \leftarrow W} \\ \mathbf{0}^\top & 1 \end{bmatrix},$$

where $R_{H \leftarrow W}$ and $t_{H \leftarrow W}$ denote the rotation and translation from the world to the hand-local canonical frame. Similarly, the wrist-mounted camera extrinsics are expressed with respect to $\{H\}$ as $\mathbf{T}_H^C = [R_{C \leftarrow H} \mid t_{C \leftarrow H}]$, enabling standard projection into $\{C\}$.

Rationale. Performing optimization and prediction in this canonical hand-local frame removes global translation and rotation degrees of freedom, thereby improving numerical stability and convergence. It also normalizes all subjects into a unified representation, facilitating cross-participant alignment and enhancing generalization. Finally, canonicalizing meshes in $\{H\}$ ensures that our MeshVQ-VAE quantization and multitask predictor operate on geometry that is invariant to camera placement or donning/doffing variations, yielding more robust supervision and transferability.

B.2 Shape Parameter Calibration (MANO β)

In this section, we describe in detail how to apply the approach of [40] to calibrate the MANO parameter β for participants' hands before the annotation optimization step. We first calibrate β by optimizing them using the following composite objective. This calibration ensures that the hand mesh is closely aligned with the ground-truth markers in the world frame, which is crucial for reducing the optimization difficulty in later stages. The resulting calibrated shape parameters β^* are fixed for subsequent optimization of the pose parameters θ and the rigid transformations.

$$\mathcal{L}_{\text{shape}}(\beta, \theta) = \omega_{3D} \mathcal{L}_{\text{marker}}^{3D} + \omega_{2D} \mathcal{L}_{\text{marker}}^{2D} + \omega_{\text{mask}} \mathcal{L}_{\text{mask}} + \omega_{\text{anat}} \mathcal{L}_{\text{anat}}(\beta, \theta) + \omega_{\text{reg}} \mathcal{L}_{\text{reg}}(\beta, \theta). \quad (5)$$

Here, $\mathcal{L}_{\text{marker}}^{3D}$ enforces 3D consistency between mocap markers in the world coordinate system and the corresponding mesh vertices in the hand-local frame, while $\mathcal{L}_{\text{marker}}^{2D}$ provides projection-consistency supervision in the image plane. The marker losses primarily constrain *bone lengths* and skeletal proportions, whereas the mask term $\mathcal{L}_{\text{mask}}$ constrains the *global hand shape/fatness* via silhouette alignment.

Let $J_m^{\text{gt}, W} \in \mathbb{R}^{N_j \times 3}$ be the 3D ground-truth marker coordinates in the world frame, and let $[R_{\text{kine}} \mid t_{\text{kine}}]$ and K denote the Kinect extrinsics and intrinsics, respectively. Denote by $\text{MANO}(\beta, \theta)$

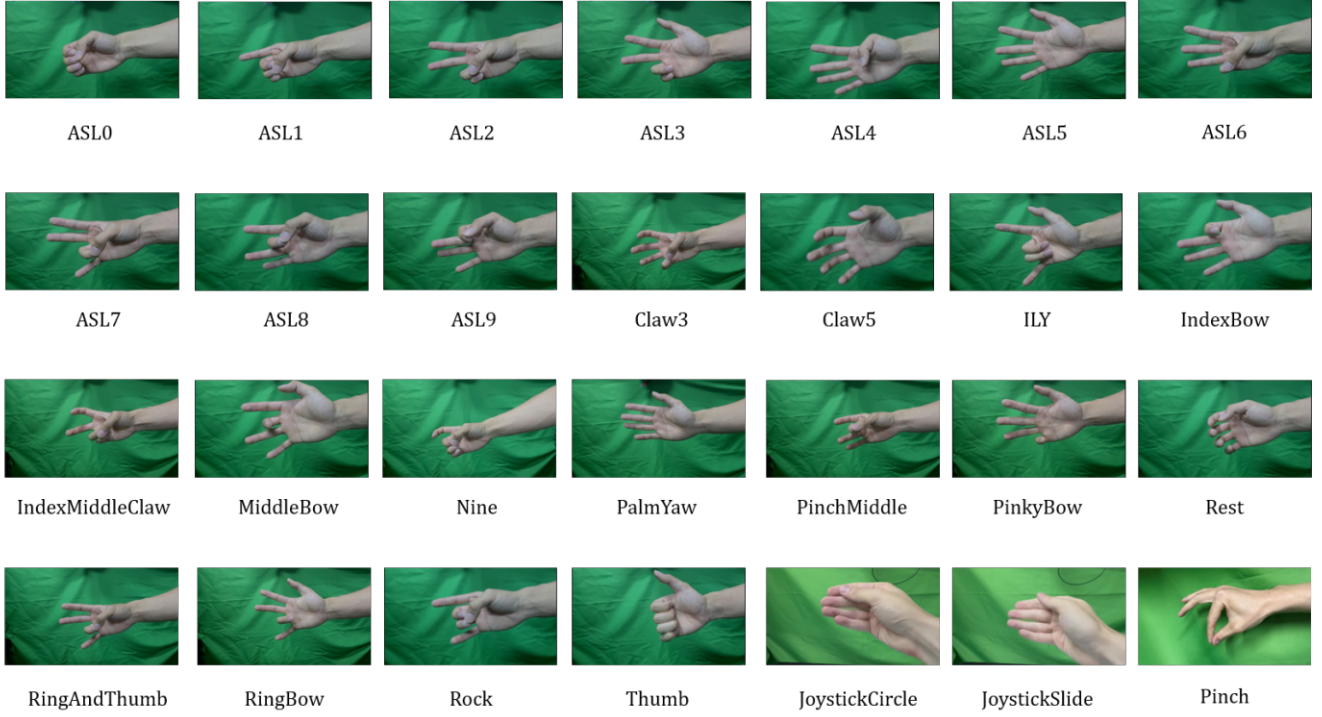


Figure 21: Mid-air Series Gestures

differentiable MANO layer producing the hand mesh in the hand-local frame and by $J_v^{\text{pred},C}$ the corresponding 3D mesh joint locations. We define the conversion between world and local coordinate systems as follows:

$$J_m^{\text{gt},C} = R_{\text{kine}} J_m^{\text{gt},W} + t_{\text{kine}}, \quad (6)$$

$$\mathcal{L}_{\text{marker}}^{\text{3D}}(\beta, \theta) = \frac{1}{N_j} \sum_{j=1}^{N_j} \|J_{v,j}^{\text{pred},C} - J_{m,j}^{\text{gt},C}\|_2^2, \quad (7)$$

$$\mathcal{L}_{\text{marker}}^{\text{2D}}(\beta, \theta) = \frac{1}{N_j} \sum_{j=1}^{N_j} \|\Pi_K(J_{v,j}^{\text{pred},C}) - \Pi_K(J_{m,j}^{\text{gt},C})\|_2^2, \quad (8)$$

where $\Pi_K(\cdot)$ denotes projection with intrinsics K .

Note that the 3D marker loss involves the ground-truth markers in the world frame and the corresponding mesh vertices in the local frame. To obtain the world-to-local transformation matrix, we use the coordinate system conversion function to map the ground-truth markers into the hand-local frame. However, this transformation matrix is not directly applicable for converting the predicted mesh from the hand-local frame to the world frame. Instead, we use this computed matrix as an initial guess for optimization, and then maintain a delta transformation that includes a delta rotation matrix and a delta translation vector. This optimization process refines the transformation matrix, which is then used to project the predicted mesh into the world frame for final supervision against the 3D marker ground truth.

The binary hand masks are obtained by a two-stage pipeline (YOLO detection followed by SAM2 segmentation). Let M_{gt} be the

resulting ground-truth mask and $\tilde{M}(\beta, \theta)$ the predicted silhouette rendered by projecting the mesh produced by $\text{MANO}(\beta, \theta)$. We use a BCE+Dice hybrid loss:

$$\mathcal{L}_{\text{mask}}(\beta, \theta) = \lambda_{\text{bce}} \text{BCE}(\tilde{M}, M_{\text{gt}}) + \lambda_{\text{dice}} (1 - \text{Dice}(\tilde{M}, M_{\text{gt}})). \quad (9)$$

The anatomical prior $\mathcal{L}_{\text{anat}}(\beta, \theta)$ follows MANO's joint-limit and plausibility constraints, and $\mathcal{L}_{\text{reg}}(\beta, \theta)$ regularizes parameter magnitudes. After convergence, the calibrated shape β^* is fixed for the subsequent stages of our pipeline.

We use WiLoR [76] to process the calibration sequence of the hand image to provide the initial values β_{init} and θ_{init} . The calibrated shape parameters β^* will be used as fixed values for the subsequent optimization of this participant.

B.3 Pre-training Dataset Construction and Statistics (for GNN initialization and Hand-VQ-VAE)

The pie chart in Fig. 22 represents the distribution of various datasets used for GNN initialization and Hand-VQ-VAE prior construction. The total number of samples across all datasets is 433,296. The largest portion of the data comes from the GigaHand dataset, contributing 54.6% (236,372 samples). Other significant datasets include HanCo (18.9%, 81,984 samples) and DexYCB(15.1%, 65,471 samples). Smaller contributions come from Interhand (5.6%, 24,141 samples), HO3D V2 (2.1%, 9,219 samples), and HO3D V3 (3.7%, 16,109 samples).

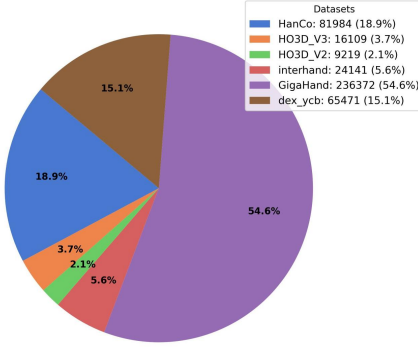


Figure 22: Distribution of various datasets used for GNN initialization and Hand-VQ-VAE prior construction.

B.4 Fisheye Background Replacement Data Augmentation Details

To introduce diversity into the background and improve the model’s generalization across different environments, we design a background replacement strategy. The algorithm first randomly selects a background image I_{pano} from a pre-downloaded 360° panoramic image database $\mathcal{D}_{\text{pano}}$, which contains over 1550 high-quality indoor panorama images. To simulate different viewpoints, a random 3D rotation matrix R_{view} is generated. This step ensures that the background is observed from various angles, enriching the training data diversity.

The selected panoramic image I_{pano} is then transformed into a fisheye perspective based on the calibrated fisheye camera model C_{fish} and the virtual camera pose R_{view} . The projection transformation process is as follows:

B.4.1 (Ray Generation for Fisheye View: For each pixel $(u_{\text{fish}}, v_{\text{fish}})$ of the target fisheye image (with dimensions $H_{\text{out}} \times W_{\text{out}}$), the inverse projection function \mathcal{P}^{-1} of the fisheye camera model is used to compute the unit observation ray $\vec{d}_{\text{cam}}(u_{\text{fish}}, v_{\text{fish}})$ in the camera’s 3D coordinate system:

$$\vec{d}_{\text{cam}}(u_{\text{fish}}, v_{\text{fish}}) = \mathcal{P}^{-1}(u_{\text{fish}}, v_{\text{fish}}, 1)$$

The collection of all rays forms the ray bundle $\mathbf{D}_{\text{cam}} \in \mathbb{R}^{H_{\text{out}} \times W_{\text{out}} \times 3}$.

B.4.2 Ray Bundle Transformation: The ray bundle \mathbf{D}_{cam} in the camera’s standard coordinate system is then transformed using the randomly generated rotation matrix R_{view} to obtain the ray bundle $\mathbf{D}_{\text{world}}$ in the panoramic world coordinate system. The transformation for each pixel’s corresponding ray is:

$$\vec{d}_{\text{world}}(u_{\text{fish}}, v_{\text{fish}}) = R_{\text{view}} \vec{d}_{\text{cam}}(u_{\text{fish}}, v_{\text{fish}})$$

B.4.3 World Coordinates to Spherical Coordinates Conversion: For each ray $\vec{d}_{\text{world}} = (x_w, y_w, z_w)^T$, it is converted into spherical coordinates (λ, ϕ) , where:

$$\lambda = \text{atan2}(x_w, z_w)$$

$$\phi = \text{asin}\left(\frac{y_w}{\|\vec{d}_{\text{world}}\|_2}\right)$$

Here, λ is the longitude (azimuth) and ϕ is the latitude (elevation).

B.4.4 Spherical Coordinates to Panoramic Image Mapping: The spherical coordinates (λ, ϕ) are mapped to the 2D pixel coordinates $(u_{\text{pano}}, v_{\text{pano}})$ in the selected panoramic image I_{pano} using equirectangular projection:

$$u_{\text{pano}} = \left(\frac{\lambda}{2\pi} + \frac{1}{2}\right) \cdot (W_{\text{pano}} - 1)$$

$$v_{\text{pano}} = \left(\frac{1}{2} - \frac{\phi}{\pi}\right) \cdot (H_{\text{pano}} - 1)$$

B.4.5 Background Pixel Resampling and Composition: The corresponding pixel colors from the panoramic image I_{pano} are extracted using bilinear interpolation at the coordinates $(u_{\text{pano}}, v_{\text{pano}})$. The final fisheye background image $I_{\text{bg_fish}}$ is obtained by combining the resampled pixels with the hand mask M_{hand} and the original hand foreground I_{hand} :

$$I_{\text{final}} = I_{\text{bg_fish}} \odot M_{\text{hand}} + I_{\text{hand}} \odot (1 - M_{\text{hand}})$$

where \odot denotes element-wise multiplication.

This projection transformation process generates a background-replaced image that is visually consistent with fisheye lens distortion, improving the model’s performance in complex real-world scenarios.

C Comparison with Baseline Methods

In this section, we present additional comparisons between WRISTP² and existing methods for 3D hand pose reconstruction and contact/pressure estimation. All numbers are reported on the held-out test split consisting of sequences from five subjects for whom we collected synchronized head-mounted and environment-mounted video, along with full 3D hand pose and pressure annotations. All methods are evaluated on the same test split as WRISTP² without any additional training or fine-tuning. Our goal is to systematically compare wrist-mounted sensing against state-of-the-art head-mounted and environment-mounted approaches, and to analyze their robustness under different illumination. We acknowledge that fine-tuning these baselines on our dataset would yield a fairer comparison, and we leave this investigation to future work.

C.1 Experimental Setup for Baseline Methods

Baselines. We consider three representative baselines: *MediaPipe* [53], *WiLoR* [76], and *PressureVision++* [21]. *MediaPipe* is a widely used lightweight hand pose estimator in HCI research and is often employed to obtain proxy ground-truth 2D/3D hand joint annotations from RGB images. However, as our experiments show, its 3D accuracy is limited in our setting, which calls into question the common practice of using its predictions as training labels for downstream models. *WiLoR* is a model-based state-of-the-art approach that directly regresses 3D MANO hand parameters from monocular RGB frames, and constitutes a strong environment-/head-mounted baseline for pose reconstruction.

For pressure estimation, although *EgoPressure* [117] reports strong single-view hand pressure prediction performance, neither its code nor its dataset is publicly available. We therefore adopt its predecessor, *PressureVision++*, as our baseline. *PressureVision++* takes an RGB image of the hand as input and regresses a per-pixel pressure map in kPa. Because our dataset does not provide pixel-wise

pressure annotations for the head-mounted camera (and obtaining such annotations would be non-trivial), we evaluate PressureVision++ only on binary contact prediction for both environment and head views, and do not report dense pressure errors for this method. For all baselines, we report metrics for both head-mounted and environment-mounted camera views whenever applicable and further break down the results by illumination condition.

Evaluation protocol. We evaluate 3D hand pose reconstruction in the hand-local frame using the same metrics as in the main paper: MPJPE, PA-MPJPE, PVE, PA-PVE, and MJAE. To study robustness to lighting, we report results under three illumination conditions (High/Medium/Low, denoted H/M/L) as well as the overall performance across all conditions.

For contact/pressure estimation we focus on binary contact prediction. A mesh vertex is considered in contact if the maximum of its per-vertex pressure exceeds 10 g; a sample is classified as contact if at least one vertex is in contact. Given this ground-truth labeling, we evaluate each method using Accuracy (Acc), Precision (Prec), Recall (Rec), and F1-score (F1). Unless otherwise stated, all metrics are reported on the held-out test set.

C.2 Quantitative Results

Pose reconstruction across illumination conditions. Table 10 summarizes pose reconstruction accuracy under different illumination conditions for the environment view baselines and our wrist-mounted model. Across all settings, WRISTP² achieves the lowest errors on MPJPE, PA-MPJPE, PVE, PA-PVE, and MJAE.

Aggregated over all illumination conditions (*All row*), WRISTP² reduces MPJPE from 46.8 mm (MediaPipe) and 15.0 mm (WiLoR) to 3.0 mm, corresponding to roughly 15× and 5× lower error, respectively. PA-MPJPE decreases from 23.8 mm and 9.2 mm to 2.3 mm, and MJAE drops from 36.8° and 13.8° to 3.4°. Similar trends hold for the vertex-based metrics PVE and PA-PVE.

The benefits of wrist-mounted sensing become even more apparent under Low illumination. In this regime, WRISTP² attains 3.2 mm MPJPE and 3.5° MJAE, while MediaPipe and WiLoR incur 45.2 mm / 36.2° and 15.4 mm / 13.8° errors, respectively.

Effect of camera view. Table 11 compares pose accuracy across different camera configurations when aggregating over all illumination conditions. For MediaPipe and WiLoR, we evaluate both environment and head-mounted views, while WRISTP² uses only the wrist-mounted camera.

The performance of environment- and head-view remains comparable. For instance, WiLoR’s error shifts from 15.0 mm MPJPE (env) to 15.3 mm (head), and MJAE increases from 13.8° to 14.8°. This indicates that the distinction between these two external perspectives is minimal. In contrast, WRISTP² achieves 3.0 mm MPJPE and 3.4° MJAE from the wrist-mounted view, outperforming both baseline configurations. We attribute this performance gap to the inherent advantages of the wrist-mounted perspective: its proximal placement enables high-fidelity observation of fine-grained finger movements, while the viewing angle reduces self-occlusion compared to external views.

Contact and pressure estimation. Table 12 reports binary contact prediction metrics for PressureVision++ and WRISTP², split by illumination and view. Under the environment view, PressureVision++ achieves reasonably high precision (92.4% on average) but very low recall (20.9%), resulting in an F1-score of only 34.1%. This pattern indicates that PressureVision++ behaves as a highly conservative classifier that predicts contact only in very confident cases and misses the majority of true contact events.

In contrast, WRISTP² attains both high precision (92.6%) and very high recall (97.9%) on average, yielding a 95.2% F1-score. The difference is most striking under Low illumination: for the environment view, PressureVision++ reaches 31.5% accuracy but only 0.66% recall and 1.32% F1-score, essentially failing to detect contacts, whereas WRISTP² maintains 97.3% accuracy, 97.9% recall, and 94.2% F1-score. For the head-mounted view, PressureVision++ degrades further to an average recall of 7.3% and F1-score of 13.5%. These results highlight that reliable contact prediction from distant views is highly challenging, especially under poor lighting, and that our wrist-mounted configuration is crucial for capturing fine-grained contact events.

C.3 Qualitative Results

Pose reconstruction. Figure 23 provides qualitative comparisons for 3D hand pose reconstruction under challenging illumination and wrist orientations. Each example shows input camera images from distinct views, the ground-truth mesh, and predictions from MediaPipe, WiLoR, and WRISTP². The baselines frequently exhibit depth ambiguities, finger interpenetration, and noisy fingertip articulation, especially under low illumination. In contrast, WRISTP² produces meshes that closely match the ground truth in both global pose and fine-grained articulation, consistent with the quantitative advantages reported in Tables 10 and 11.

Contact and pressure estimation. Figure 24 shows planar interaction examples with contact and pressure maps. For each scene, we visualize ground-truth pressure, followed by the predictions of WRISTP². Notably, PressureVision++ exhibits overly conservative predictions, predicting zero pressure across all these scenes and thus cannot be included in the figure. Consistent with Table 12, WRISTP² produces contact regions that closely align with the ground truth and captures coherent pressure patterns across the fingers and palm. PressureVision++ often misses light contacts at the fingertips, predicts overly sparse contact regions, or fails completely under low illumination, leading to very low recall and F1-scores.

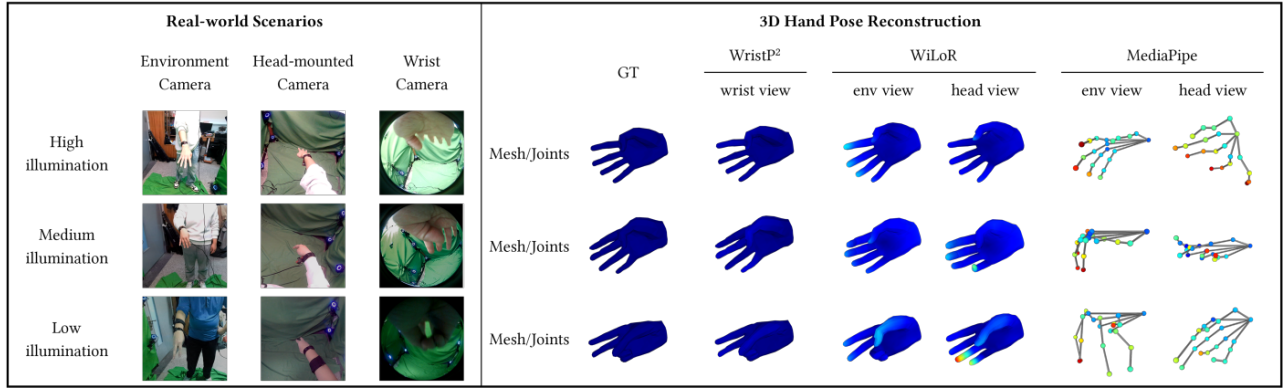
Failure cases. Finally, Figure 25 highlights typical failure cases for WRISTP². Severe occlusions, motion blur, and hand poses far outside the training distribution can still lead to noticeable errors in pose or pressure estimation. These examples complement our quantitative results and suggest promising directions for future work, such as combining wrist-mounted cameras with additional sensing modalities or incorporating explicit reasoning about object appearance and contact dynamics.

D Additional Qualitative Results

As a supplement to Section 6, the model’s predictions for 15 different mid-air interaction gestures at varying wrist pitch angles are

Table 10: Pose accuracy across illumination conditions (env view). Position errors are reported in mm; MJAE in degrees (°). Lower is better for all metrics. PVE and PA-PVE are not available for MediaPipe and are marked as “–”.

Illumination	Method	MPJPE	PA-MPJPE	PVE	PA-PVE	MJAE [°]
High (H)	MediaPipe	47.8	23.5	–	–	36.5
	WiLoR	14.6	9.2	14.1	9.0	13.6
	WRISTP ² (Ours)	2.8	2.1	2.8	2.2	3.2
Medium (M)	MediaPipe	47.0	24.3	–	–	37.7
	WiLoR	15.2	9.3	14.6	9.1	14.1
	WRISTP ² (Ours)	3.1	2.3	3.0	2.4	3.5
Low (L)	MediaPipe	45.2	23.4	–	–	36.2
	WiLoR	15.4	9.1	14.9	8.8	13.8
	WRISTP ² (Ours)	3.2	2.3	3.1	2.4	3.5
All	MediaPipe	46.8	23.8	–	–	36.8
	WiLoR	15.0	9.2	14.5	9.0	13.8
	WRISTP ² (Ours)	3.0	2.3	2.9	2.3	3.4

**Figure 23: Qualitative comparison on 3D hand pose reconstruction. From left to right: input images from the environment camera, head-mounted camera, and wrist camera, ground-truth mesh, and pose predicted by WRISTP² (ours, reconstructed mesh), WiLoR (reconstructed mesh), and MediaPipe (3D joints, no mesh support). Per-vertex or per-joint position errors are visualized as color-coded overlays on the predicted meshes or 3D joints, utilizing a consistent jet colormap with a minimum value (vmin) of 0 mm and a maximum value (vmax) of 100 mm. Both MediaPipe and WiLoR suffer from inaccurate joint configurations, while MediaPipe additionally exhibits finger entanglement that results in physically implausible 3D hand pose reconstructions. Conversely, WRISTP² better preserves fingertip articulation and reduces depth ambiguities.**

presented in Fig. 26, demonstrating the model’s high accuracy in predicting complex 3D hand postures.

E Specification of Multi-Finger Combinations in Pressure Control

In Section 7.4, thirteen different finger combinations were randomly selected, encompassing single-finger, two-finger, three-finger, four-finger, and five-finger configurations. These combinations represent common and natural finger postures in planar hand interactions, with the specific combinations illustrated in Fig. 27.

Table 11: Effect of camera view on pose accuracy (All illumination). Position errors are reported in mm; MJAE in degrees (°). Lower is better.

Method	View	MPJPE	PA-MPJPE	PVE	PA-PVE	MJAE (°)
MediaPipe	env	46.80	23.80	–	–	36.80
	head	39.10	19.40	–	–	31.20
WiLoR	env	15.00	9.20	14.50	9.00	13.80
	head	15.30	9.30	14.70	9.20	14.80
WRISTP ² (Ours)	wrist	3.00	2.30	2.90	2.30	3.40

Table 12: Contact prediction performance under different lighting conditions and camera views. We report Accuracy (Acc), Precision (Prec), Recall (Rec), and F1-score (%) for PressureVision++ and WRISTP² (ours). Bold numbers indicate the best results under each lighting condition for the env view.

View	Method	Lighting	Acc	Prec	Rec	F1
env	PressureVision++	High (H)	43.3	87.9	27.6	42.0
		Medium (M)	56.0	98.0	31.3	47.4
		Low (L)	31.5	100.0	0.7	1.3
		Avg.	44.1	92.4	20.9	34.1
head	PressureVision++	High (H)	34.4	96.3	12.4	21.9
		Medium (M)	40.1	80.0	7.5	13.7
		Low (L)	31.1	0.0	0.0	0.0
		Avg.	35.3	90.5	7.3	13.5
wrist	WRISTP ² (Ours)	High (H)	98.7	96.1	98.5	97.3
		Medium (M)	97.0	90.1	97.3	93.6
		Low (L)	97.3	90.7	97.9	94.2
		Avg.	97.7	92.6	98.0	95.2

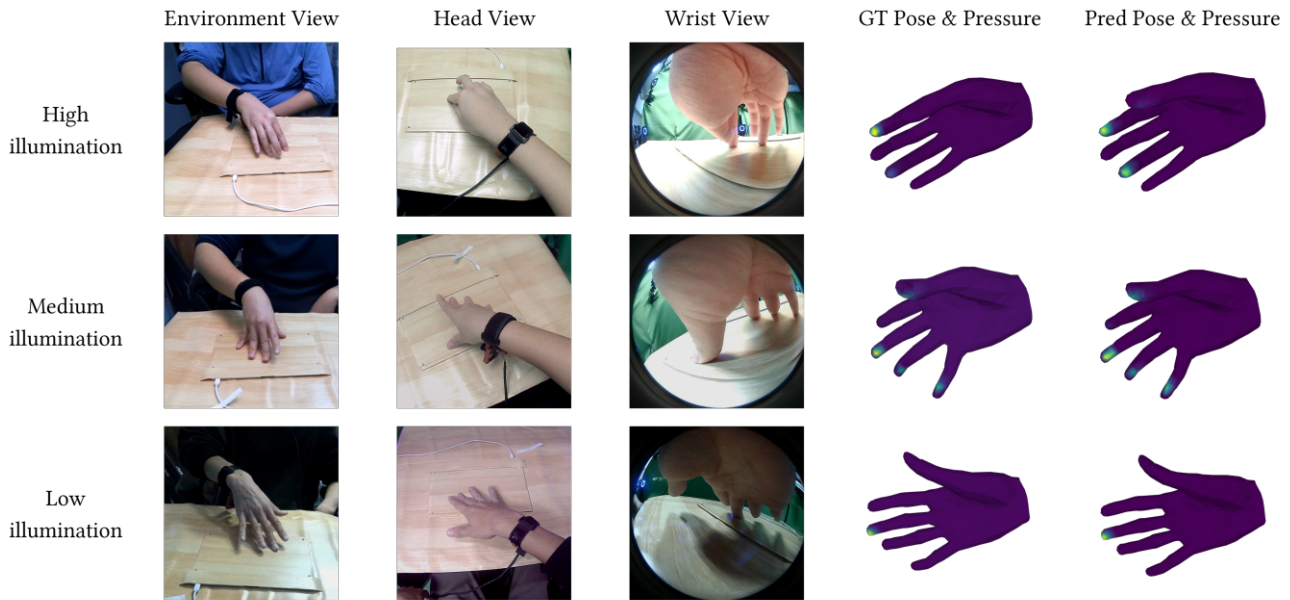


Figure 24: Qualitative comparison on contact and pressure estimation. From left to right: input images from distinct views, ground-truth hand meshes overlaid with pressure visualization, and prediction of WRISTP². WRISTP² accurately localizes contact regions and reproduces plausible pressure magnitudes. Meanwhile, PressureVision++ predicts all-zero pressure values across the 2D pixel space for both the environment view and head view in all three cases, and is not included in the figure.

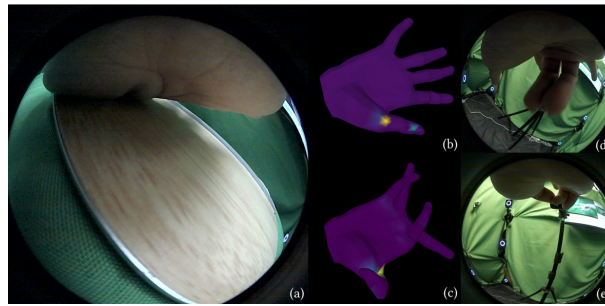


Figure 25: Representative failure cases of WRISTP². Under challenging visual conditions, both pose and pressure estimation can degrade. (a) Complete occlusion of multiple finger segments leads to a MPJPE of 31.7 mm and notable pressure misestimation, with ground-truth and predicted pose/pressure reconstructions shown in (b) and (c), respectively. Specifically, the occlusion of the thumb pad in (c) stems from the 2D rendering angle, and the model predicts no pressure here. (d) Partial occlusion of the index finger coupled with motion blur on the middle and ring fingers results in a MPJPE of 18.1 mm. (e) Occlusion at the base of the middle finger and full occlusion of the pinky yield a MPJPE of 19.4 mm. We include these examples for transparency and to motivate future research on handling such challenging scenarios.

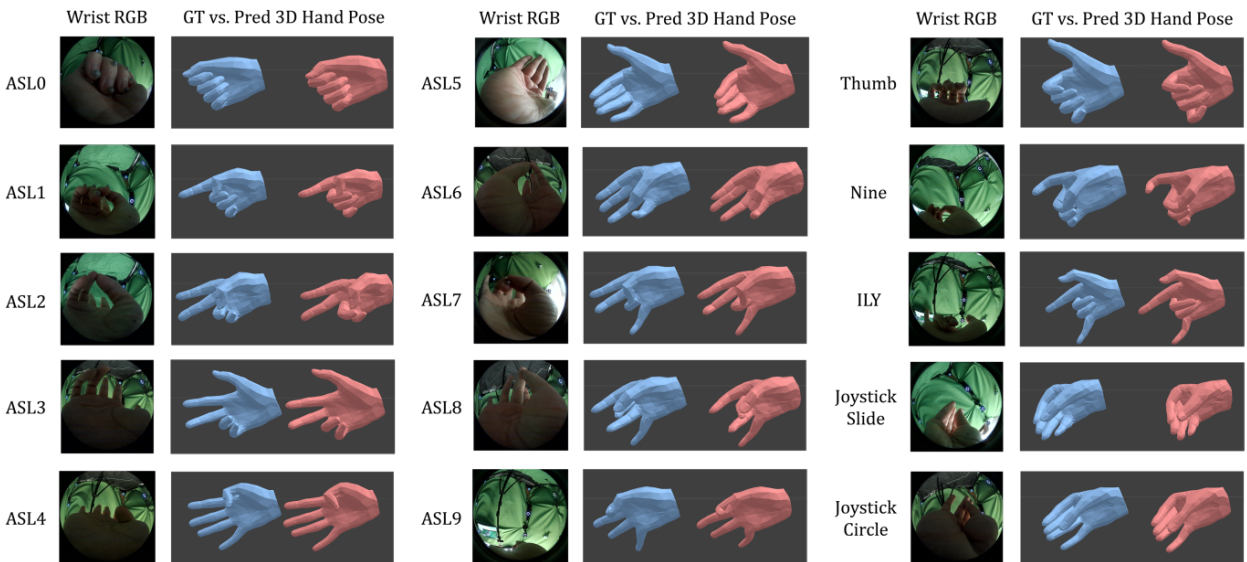


Figure 26: Additional qualitative results of mid-air hand poses. Images of wrist camera views for various mid-air gestures, with a comparison between the ground truth 3D hand poses (in blue) and the predicted 3D hand poses (in red).



Figure 27: The 13 finger combinations in the Multi-finger Pressure Control user study. The combinations of single, double, triple, quadruple, and quintuple finger configurations represent natural and commonly used finger postures in planar hand interactions.